Nonlinear Dynamics (2026) 114:618
https://doi.org/10.1007/s11071-026-12443-6

RESEARCH

Sloshing-height estimation for liquid-filled containers under four-dimensional motions including spatial translation and rotation about a fixed direction: modelling and experimental validation

Roberto Di Leva[1] · Simone Soprani[2] · Gianluca Palli[2] · Luigi Biagiotti[3] · Marco Carricato[1]

Received: 29 July 2025 / Revised: 21 January 2026 / Accepted: 3 March 2026

Abstract
Sloshing is the nonlinear dynamical behaviour of a liquid undergoing free-surface oscillations within an accelerated, partially filled vessel. In industrial scenarios, when liquid-filled containers are transported between stations in processing or packaging lines, liquid sloshing often needs to be limited to prevent undesirable effects, such as spillage or disruption of operations. In this case, reliable and near real-time models are needed to optimize the liquid behavior under specific container motions. Since typical pick-and-place operations involve 3D translational paths combined with a rotation about a fixed-orientation axis, this paper extends the sloshing-height-estimation models previously developed by the authors for translational motions and cylindrical containers, to take into account an additional rotation either about a vertical axis (known as *SCARA motion*) or around a horizontal axis with a fixed direction (denoted as *Tilting motion*). The presented approach, based on two equivalent discrete mechanical models, i.e. the mass-spring-damper and the pendulum, exhibits meaningful merits: it is computationally cheap, it requires no experimental assessment of the model parameters, and it needs no external sensor readings. Several sloshing-height formulations are proposed for the two models and an extensive experimental campaign is conducted to assess the effectiveness and the limitations of the most promising formulations for both models. Experiments cover configurations in which the ratio of the static liquid height to the container radius ranges from 0.6 to 1.6, and including dynamic motions with container accelerations up to 7.2m/s^2 and 11.0rad/s^2. All experimental data sets are distributed on a public repository for future use by the community.

Keywords Liquid Sloshing · Sloshing-height Estimation · Model Validation · Experimental Analysis · SCARA Motion · Tilting Motion

1 Introduction

Sloshing is the oscillatory behavior of a liquid inside a container subject to an acceleration. The study of liquid sloshing is crucial in many engineering fields, ranging from the aerospace and automotive sectors to the packaging-line industry. In particular, in pharmaceutical and food-and-beverage production lines, the transport of liquids usually takes place in open cylindrical vessels or vials. These containers are often required not only to follow $1D$ or $2D$ translational motions along transfer conveyors, but also to be picked and placed between stations by industrial robots, which usually perform $3D$ translational motions combined

✉ Marco Carricato
marco.carricato@unibo.it

Roberto Di Leva
roberto.dileva@unibo.it

Simone Soprani
simone.soprani2@unibo.it

Gianluca Palli
gianluca.palli@unibo.it

Luigi Biagiotti
luigi.biagiotti@unimore.it

[1] Department of Industrial Engineering, University of Bologna, Viale del Risorgimento 2, Bologna 40136, Italy

[2] Department of Electrical, Electronic and Information Engineering "Guglielmo Marconi", University of Bologna, Viale del Risorgimento 2, Bologna 40136, Italy

[3] Department of Engineering "Enzo Ferrari", University of Modena and Reggio-Emilia, Via Vivarelli 10, Modena 41125, Italy

Published online: 28 April 2026

with a rotation about a constant-orientation axis, which can be either vertical (SCARA motion [1]) or horizontal (tilting motion [2, 3]). Depending on the acceleration the container is subjected to (usually called *excitation*), the sloshing behavior of the liquid can produce spillage, or leave deposits on the container walls, which may compromise the subsequent operations (e.g. freeze-drying operations) or cause aesthetic defects.

In general, predicting the sloshing height reached by the liquid is crucial to plan the optimal trajectory that the manipulation system of the container has to execute. Finite Element Methods (FEM) can be used to predict the liquid dynamics [4], [5], but they are computationally expensive and require a preliminary generation of a mesh able to replicate the liquid behavior. A mesh-less approach is offered by Computational Fluid Dynamics (CFD) softwares, such as the ones employing Smooth Particle Hydrodynamics [6, 7]: they offer high adherence with reality, but they are also computationally demanding. Theoretical approaches involve the direct numerical integration of the Navier-Stokes equations governing liquid dynamics. In this field, the authors of [8] adopted the Volume-of-Fluid technique, but the computational burden is still very high (e.g. 265h of CPU time to simulate 50s of motion). Other works focus on reducing the Navier-Stokes equations to a set of ordinary differential equations (ODEs), which are easier to integrate numerically. In [9], the coefficients of the nonlinear sloshing dynamics model presented in [10] are provided for rectangular containers subject to $3D$ motions, but the resulting formulation is complex and difficult to use, and indications are not provided about the computational burden. In [11], the Navier-Stokes equations are simplified by applying the shallow-water assumption, where the vertical velocity is negligible compared to the horizontal one; this approach demonstrates its efficacy for shallow-water sloshing, but it is still computationally demandig (roughly 40mins to simulate 5s of sloshing). Model-free methods based on machine learning methodologies are presented in [12] and [13], where, starting from data collection, predictive algorithms are built to assess the behavior of the liquid inside a cylindrical container. This technique, though very powerful, requires experiments to be run beforehand to acquire suitable datasets, and it requires a non-negligible computational effort.

A much faster alternative to all aforementioned approaches is represented by equivalent discrete mechanical models, which provide reliable predictions of the sloshing height without the expensive computational effort of FEM, CFD, direct-integration and machine-learning techniques. The literature identifies two main (lumped-parameter) discrete approaches for modelling sloshing dynamics inside a cylindrical container subjected to a $2D$ planar motion involving a $1D$ horizontal translation (called 'lateral' excitation) and/or a rotation about a horizontal axis perpendicular to the former (called 'pitching' or 'tilting' excitation) [14]. In both cases, the overall liquid mass is replaced by a mass that moves rigidly with the container and a series of masses that move with respect to (w.r.t.) it, thus representing the portion of oscillating liquid. The difference in the two approaches lies in how the sloshing masses are coupled to the container: in one case through springs and dashpots, thus forming a series of mass-spring-damper (MSD) systems; in the other case through oscillating pendulums (PEN). Discrete models can be built based on either linear or (weakly) nonlinear sloshing theory. The former accurately predicts natural frequencies, wave heights, and hydrodynamic pressures, forces, and moments under lateral or pitching excitation, provided that the free surface remains planar with a nodal diameter perpendicular to the excitation. However, the linear sloshing theory fails to capture large-amplitude effects (such as the vertical motion of the center of mass (CoM) and the non-planarity of the free surface), which require the theory of weakly nonlinear oscillations for quantitative analysis, with nonlinearity arising primarily from free-surface boundary conditions [14].

In [15], optimized and non-optimized 1D trajectories are compared using the PEN model; however, the actual sloshing height is not computed and no experimental validation is provided. The PEN model is also used in [16–18], where compensatory actions are performed to suppress sloshing under $3D$ translational motions. The sloshing-height prediction is based on the tangent functions of the pendulum angles and the assumption that the liquid free surface remains planar. Experiments involve a cylindrical container subjected to accelerations up to 2.0m/s^2. In [19, 20], the PEN model is used to plan 2D motions with accelerations no higher than 2.0m/s^2. The sloshing height is still computed through the tangent functions of the pendulum angles and the assumption of a planar liquid surface. In [21], a constraint-based online algorithm for anti-spillage 3D trajectory generation is introduced; the sloshing magnitude is evaluated based on the pendulum angles.

The MSD model is used in [22] for sloshing suppression in a rectangular container following a $1D$ motion with a maximum acceleration of 1.5m/s^2: the sloshing height is formulated as a function of the sloshing-mass displacements. In [23, 24], spacecraft control is studied in planar motion (2D translation plus 1D rotation) using sloshing-mass displacements to characterize the liquid behavior. However, sloshing height is not directly formulated, and results are purely theoretical, with no experimental validation.

A novel approach to compute the sloshing height based on the MSD model is presented in [25], and validated for cylindrical containers performing 1D translational motions with accelerations up to 12m/s^2. The main merits of this formulation are its direct physical correspondence with the actual liquid peak and its applicability to both the linear and the

nonlinear MSD model [26]. The technique proposed in [25] is exploited in [27] and [28] to plan anti-sloshing trajectories and in the software application [29] to execute simulations of liquid sloshing in cylindrical and rectangular containers. The extension of the approach in [25] to $2D$ translational motions is experimentally validated in [30], with accelerations up to 9.5m/s^2, and used in [31] to plan corresponding anti-sloshing motion laws. The extension of the formulation in [25] to $3D$ translational motions is reported and experimentally validated in [32], with a maximum acceleration of 7.4m/s^2.

To the best of the authors' knowledge, the literature lacks:

- accurate and computationally efficient methods for estimating sloshing height under arbitrary spatial translations and rotations about fixed-direction axes;
- a comprehensive theoretical and experimental comparison of the accuracy achieved by discrete models (MSD, PEN) and their variants.

Thus, the aim of this paper is:

- to extend the models developed in [18, 25, 32] to $4D$ motions of a cylindrical container comprising $3D$ spatial translations and $1D$ rotations about fixed-orientation axes, either vertical (*SCARA motions*) or horizontal (*tilting motions*);
- to provide a physically consistent formulation of the sloshing height for both MSD and PEN models, leveraging the equivalence between discrete and continuum representations;
- to present a comprehensive comparison among the various MSD and PEN model variants, identifying the most accurate ones for the considered motion profiles;
- to support the theoretical findings with the results from an extensive experimental campaign, covering configurations in which the ratio of the static liquid height to the container radius ranges from 0.6 to 1.6, and involving motions with container accelerations up to 7.2m/s^2, and 11.0rad/s^2.

While the approach adopted in this paper to compute the sloshing height has already been applied by the authors of [25, 32] to the MSD model, its extension to the PEN model represents a novel contribution not previously addressed in the literature. It is worth mentioning that the container shape plays a critical role in both the definition and validity of the model. For instance, in parallelepiped-like containers, edge effects can significantly increase the model complexity as the dimensionality of the excitation grows. In this paper, we exclusively focus on cylindrical containers, which represent the most commonly used shapes in many industrially relevant scenarios.

Moreover, water is the liquid employed in our study due to its low viscosity, which makes it the most challenging case. As a matter of fact, low-viscosity liquids exhibit more pronounced sloshing behaviors, thereby increasing the complexity of the analysis.

The paper is structured as follows. Section 2 briefly introduces the fundamentals of the continuum formulation. Sections 3 and 4 present the model parameters and the sloshing-height formulations for the MSD and the PEN models, respectively. Section 5 qualitatively compares the two discrete models. Section 6 provides the motion equations for SCARA and tilting motions. Section 7 presents the results of the experimental campaign, providing a comparison of the accuracy achieved by the different formulations. All datasets collected during the experiments are made freely accessible to the scientific community through a public repository [33], enabling benchmarking against alternative approaches. Finally, Section 8 concludes the paper and outlines directions for future work.

2 Continuum model

The continuum model of an *ideal* liquid is briefly described in this Section as a support for the equivalence that will be imposed in Sections 3 and 4 to construct the discrete-model estimation of the liquid sloshing height. In particular, the liquid field equations provide the expression of the liquid free-surface shape, whose information is crucial to understand how the liquid CoM behaves during motion.

Consider a cylindrical container with vertical axis and radius R, filled with a liquid of mass m_F to a height h. $Oxyz$ is a reference frame with its z-axis aligned with the container axis, pointing upward and having O coinciding with the undisturbed position of the liquid CoM. The container is subjected to a harmonic excitation along the x-direction given by

$$x_c(t) = X_0 \cos \Omega t, \tag{1}$$

where X_0 and Ω are the excitation amplitude and frequency, respectively. Under the assumption of small excitation and fluid-response amplitudes, the linearized fluid field equations lead to a potential function – representing a solution to the Laplace Equation – of the form (see Chapter 2.2 of [14]):

$$\widetilde{\Phi}(r, \phi, z, t) = X_0 \Omega \sin(\Omega t) \cos\phi \times \\ \times \sum_{n=1}^{\infty} \left(\frac{\Omega^2}{\omega_n^2 - \Omega^2} \frac{2R}{\left(\xi_n^2 - 1\right)} \frac{J_1\left(\xi_n \frac{r}{R}\right)}{J_1(\xi_n)} \frac{\cosh\left[\xi_n \frac{h/2+z}{R}\right]}{\cosh\left(\xi_n \frac{h}{R}\right)} \right), \tag{2}$$

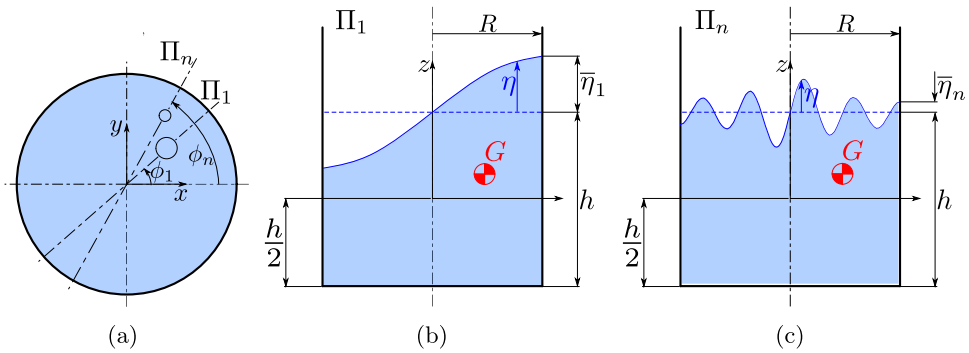

Fig. 1 Contributions of the oscillation modes to the liquid free-surface shape: (**a**) top View, (**b**) lateral view of the 1-st-mode plane Π_1, (**c**) lateral view of the n-th-mode plane Π_n

where r, ϕ, z are cylindrical coordinates in $Oxyz$, subscript n refers to the n-th radial mode, ω_n is the natural frequency associated with the n-th mode (see Eq. (12) in Section 3.2), J_1 is the first-kind Bessel function, and ξ_n is the root of the derivative of J_1, e.g.

$$\left.\frac{\partial J_1\left(\xi_n \frac{r}{R}\right)}{\partial r}\right|_{r=R} = 0, \tag{3}$$

and its values are tabulated in [34] for each n. In Eq. (2), only radial modes associated with the first circumferential mode are considered, since it can be shown that the contributions of circumferential modes higher than one to the motion of the liquid CoM are negligible [35].

The free surface shape η can be written in terms of $\widetilde{\Phi}$ as [14]

$$\eta = \frac{1}{g}\left(\frac{\partial \widetilde{\Phi}}{\partial t} - \ddot{x} r \cos\phi\right), \tag{4}$$

by imposing $z = h/2$. Several computations (better described in [26]) lead to the expression:

$$\eta(r,\phi,t) = \frac{\Omega^2}{g} x_c(t)\cos\phi \times \\ \times \sum_{n=1}^{\infty} \frac{\omega_n^2}{\omega_n^2 - \Omega^2} \frac{2R}{(\xi_n^2 - 1)} \frac{J_1\left(\xi_n \frac{r}{R}\right)}{J_1(\xi_n)}. \tag{5}$$

Equation (5) can be expressed in a more compact fashion as:

$$\eta(r,\phi,\overline{\eta}_n) = \sum_{n=1}^{\infty} \overline{\eta}_n \frac{J_1\left(\xi_n \frac{r}{R}\right)}{J_1(\xi_n)} \cos\phi, \tag{6}$$

where $\overline{\eta}_n$ is the n-th contribution to the total sloshing height on the container wall ($r = R$) and in the excitation plane ($\phi = 0$), namely:

$$\overline{\eta}_n(t) = \frac{2R\omega_n^2}{g(\xi_n^2 - 1)} \frac{\Omega^2 x_c(t)}{(\omega_n^2 - \Omega^2)}. \tag{7}$$

Equation (7) reveals that the contribution of the n-th mode does not depend on the other modes and is a function of the excitation type $x_c(t)$. This formulation can be extended to a 2D traslational container motion on an horizontal plane as:

$$\eta(r,\phi,\overline{\eta}_n) = \sum_{n=1}^{\infty} \overline{\eta}_n \frac{J_1\left(\xi_n \frac{r}{R}\right)}{J_1(\xi_n)} \cos(\phi - \phi_n), \tag{8}$$

where $\overline{\eta}_n$ still carries the information related to the excitation type, but each mode reaches its maximum value on the meridian plane identified by $\phi = \phi_n$ (Fig. 1). Since higher-order modes have a limited effect on the maximum sloshing height $\overline{\eta}$ at the container wall, we can conservatively compute $\overline{\eta}$ by assuming that the peaks of all modes occur on the same meridian plane as the first mode, namely:

$$\overline{\eta} \simeq \sum_{n=1}^{\infty} \overline{\eta}_n. \tag{9}$$

The coordinates of the liquid CoM can be computed in the reference frame shown in Fig. 1 as:

$$x_G = \frac{1}{\pi R^2 h}\int_V x\, dV = \\ = \frac{1}{\pi R^2 h}\int_0^R \int_0^{2\pi} \int_{-\frac{h}{2}}^{\frac{h}{2}+\eta(r,\phi,\overline{\eta}_n)} r^2 \cos\phi\, dz d\phi dr, \tag{10a}$$

$$y_G = \frac{1}{\pi R^2 h}\int_V y\, dV = \\ = \frac{1}{\pi R^2 h}\int_0^R \int_0^{2\pi} \int_{-\frac{h}{2}}^{\frac{h}{2}+\eta(r,\phi,\overline{\eta}_n)} r^2 \sin\phi\, dz d\phi dr, \tag{10b}$$

$$z_G = \frac{1}{\pi R^2 h}\int_V z\, dV = \\ = \frac{1}{\pi R^2 h}\int_0^R \int_0^{2\pi} \int_{-\frac{h}{2}}^{\frac{h}{2}+\eta(r,\phi,\overline{\eta}_n)} zr\, dz d\phi dr, \tag{10c}$$

where the function $\eta(r,\phi,\overline{\eta}_n)$ describes the liquid free surface, $x = r\cos\phi$, $y = r\sin\phi$, V is the liquid volume and $dV = r dz d\phi dr$.

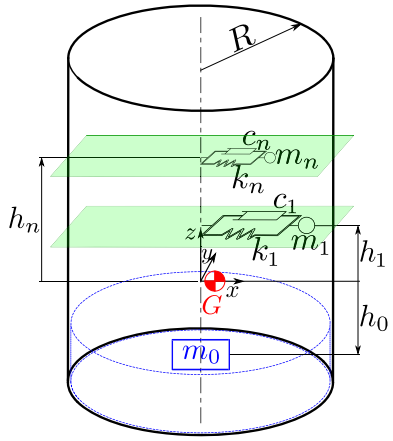

Fig. 2 Linear Mass-Spring-Damper model

By using Eq. (8), the integrals in Eq. (10) provide:

$$x_G = \frac{R}{h}\sum_{n=1}^{\infty}\frac{\overline{\eta}_n}{\xi_n^2}\cos\phi_n, \tag{11a}$$

$$y_G = \frac{R}{h}\sum_{n=1}^{\infty}\frac{\overline{\eta}_n}{\xi_n^2}\sin\phi_n, \tag{11b}$$

$$z_G = \frac{1}{4h}\sum_{n=1}^{\infty}\overline{\eta}_n^2\frac{\left(\xi_n^2-1\right)}{\xi_n^2}, \tag{11c}$$

where the integration details are reported in Appendix A.1. Equation (11) shows that the CoM continuum coordinates are functions of $\overline{\eta}_n$ and ϕ_n, which depend on the imposed excitation. The formulation of $\overline{\eta}_n$ in terms of the MSD/PEN generalized coordinates can be attained by imposing the CoM conservation between the continuum and discrete models. This approach will be described in Sections 3.3 and 4.2.

3 Mass-spring-damper model

3.1 Linear and paraboloidal mass-spring-damper models

The literature uses a Linear Mass-Spring-Damper (LMSD) model to reproduce small oscillations of the liquid, for which the vertical displacement of the liquid CoM is negligible (Fig. 2). The LMSD model comprises a mass m_0 that moves rigidly with the container, and a series of sloshing masses m_n moving w.r.t. the container and representing the sloshing modes. The motions of masses m_n are described by the generalized coordinates (x_n, y_n) and occur on different planes, with each one of them remaining parallel to the xy plane at a constant height h_n. Each mass m_n is restrained by a spring of stiffness k_n and a dashpot with damping coefficient c_n. Since the sloshing mass moves on a horizontal plane, the restoring force produced by the spring is necessary to balance inertia forces.

When the liquid oscillations are not small, but still in a weakly non-linear regime, the CoM vertical displacement cannot be neglected and a nonlinear MSD model has be to be used [14, 26] (Fig. 3). In this formulation, which we denote as Paraboloidal Mass-Spring-Damper (PMSD) model, each mass m_n slides on a paraboloidal surface and is additionally restrained by a nonlinear spring of order w. The nonlinear spring acts along the radial direction $r_n = \sqrt{x_n^2 + y_n^2}$ and produces the force $\frac{\alpha k_n r_n^{2w-1}}{R^{2w-2}}$. The parameters α, w can be conveniently tuned according to the motion type and the container dimensions [26]. It is worth noting that the paraboloidal constraint renders the spring not strictly necessary, as both the constraint and the spring provide restoring forces (the former due to gravity and the latter due to elasticity) that counterbalance inertial effects. By removing the spring (i.e.,

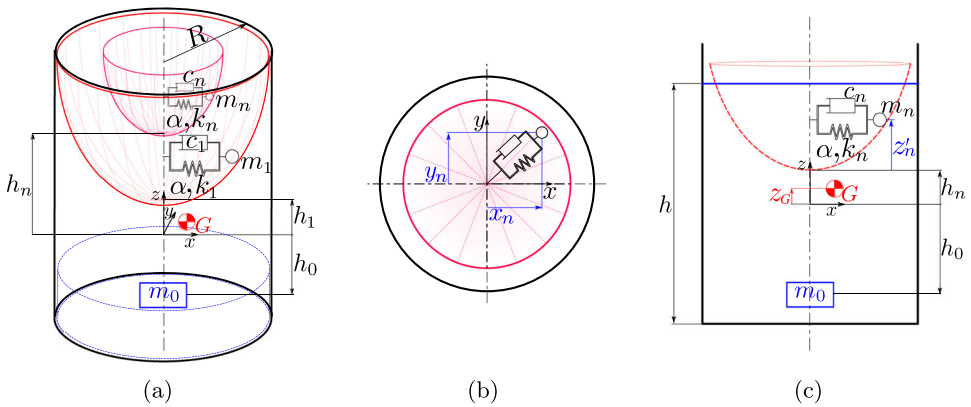

Fig. 3 Paraboloidal Mass-Spring-Damper model: (**a**) model parameters, (**b**) top view showing the n-th generalized coordinates, (**c**) CoM conservation along the vertical direction

setting α to zero), the system becomes a Paraboloidal Mass-Damper (PMD) system, which, to the best of our knowledge, has not yet been studied in the literature. This system will be examined in detail in Section 5.2.

3.2 Model parameters

The parameters of the LMSD and PMSD models can be determined by imposing a set of equivalence conditions between these models in undamped conditions and the continuum model of an ideal liquid described in Section 2 (see Chapter 5 of [14] for further details). In particular:

- the equality with the natural frequency associated with the n-th mode yields:

$$\omega_n = \sqrt{\frac{k_n}{m_n}} = \sqrt{g\frac{\xi_n}{R}\tanh\left(\xi_n\frac{h}{R}\right)}, \tag{12}$$

  where g is the gravity acceleration;
- the equality with the hydrodynamic force acting on the container wall due to translational and tilting excitations yields[1]

$$m_n = m_F\frac{2R\tanh\left(\xi_n\frac{h}{R}\right)}{\xi_n h\left(\xi_n^2-1\right)}; \tag{13}$$

$$h_n = \frac{1}{2}h\left[1-\frac{2R\tanh\left(\xi_n\frac{h}{R}\right)}{\xi_n h}\right]; \tag{14}$$

- the equality with the overall mass yields:

$$m_0 = m_F - \sum_{n=1}^{\infty} m_n; \tag{15}$$

- the conservation of the CoM height in the case of small oscillations yields:

$$m_0 h_0 + \sum_{n=1}^{\infty} m_n h_n = 0. \tag{16}$$

The damping ratio $\zeta_n = \dfrac{c_n}{2\sqrt{k_n m_n}}$ can be determined by using the experimental formula (see Section 3.2.2 of [14]):

$$\zeta_n = 0.92\sqrt{\frac{\upsilon/\rho}{\sqrt{gR^3}}} \times \left[1+\frac{0.318}{\sinh(1.84h/R)}\left(1+\frac{1-h/R}{\cosh(1.84h/R)}\right)\right], \tag{17}$$

with υ and ρ being the dynamic viscosity and density of the liquid, respectively, and assuming that the damping ratio is equal for all modes.

[1] More precisely, Eqs. (13) and (14) are obtained by imposing on the container a $1D$ harmonic translational motion along a horizontal direction and a $1D$ harmonic tilting motion about a horizontal axis, respectively.

3.3 Sloshing-height formulation

Following the approach presented in [25, 32], the formulation of the n-th sloshing height $\overline{\eta}_n$ as a function of the generalized coordinates (x_n, y_n, z_n) can be obtained by equating the coordinates of the liquid CoM in the continuum and discrete models.

The conservation of the liquid CoM along the x and y directions yields:

$$m_F x_G = m_0 x_0 + \sum_{n=1}^{\infty} m_n x_n, \tag{18a}$$

$$m_F y_G = m_0 y_0 + \sum_{n=1}^{\infty} m_n y_n. \tag{18b}$$

Substituting Eqs. (11a) and (11b) in Eqs. (18a) and (18b), and considering that $x_0 = y_0 = 0$ since mass m_0 is located on the container axis, gives:

$$m_F\frac{R}{h}\sum_{n=1}^{\infty}\frac{\overline{\eta}_n}{\xi_n^2}\cos\phi_n = \sum_{n=1}^{\infty} m_n x_n, \tag{19a}$$

$$m_F\frac{R}{h}\sum_{n=1}^{\infty}\frac{\overline{\eta}_n}{\xi_n^2}\sin\phi_n = \sum_{n=1}^{\infty} m_n y_n. \tag{19b}$$

Sufficient conditions that satisfy Eq. (19) are:

$$m_F\frac{R}{h}\frac{\overline{\eta}_n}{\xi_n^2}\cos\phi_n = m_n x_n \implies \overline{\eta}_n\cos\phi_n = \frac{\xi_n^2 h m_n}{R m_F}x_n, \tag{20a}$$

$$m_F\frac{R}{h}\frac{\overline{\eta}_n}{\xi_n^2}\sin\phi_n = m_n y_n \implies \overline{\eta}_n\sin\phi_n = \frac{\xi_n^2 h m_n}{R m_F}y_n. \tag{20b}$$

Squaring Eqs. (20a) and (20b), adding side by side, and extracting the square root yields:

$$\overline{\eta}_n = \frac{\xi_n^2 h m_n}{R m_F}\sqrt{x_n^2+y_n^2} = \frac{2R\omega_n^2}{g(\xi_n^2-1)}\sqrt{x_n^2+y_n^2}, \tag{21}$$

where the rightmost expression has been obtained by extracting m_n/m_F from Eq. (13) and using the definition of ω_n in

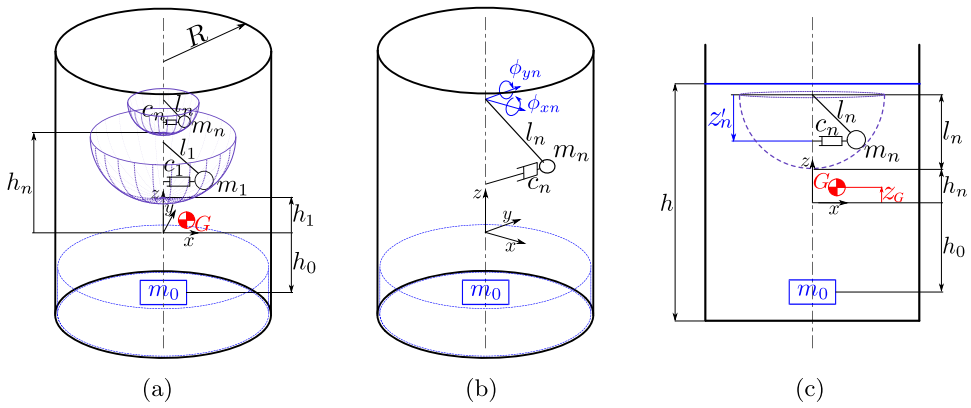

Fig. 4 Pendulum model: (**a**) model parameters, (**b**) n-th generalized coordinates, (**c**) CoM conservation along the vertical direction

Eq. (12). Equation (21) provides the contribution of the n-th sloshing mode to the overall sloshing height in Eq. (9)[2].

The conservation of the liquid CoM along the z-direction yields (see Fig. 3c):

$$\begin{aligned} m_F z_G &= m_0 h_0 + \sum_{n=1}^{\infty} m_n z_n = \\ &= m_0 h_0 + \sum_{n=1}^{\infty} m_n (h_n + z'_n), \end{aligned} \tag{22}$$

where

$$z_n = h_n + z'_n \tag{23}$$

is the vertical coordinate of the n-th sloshing mass, measured from the undisturbed-liquid CoM position. Considering Eq. (16), Eq. (22) simplifies to:

$$m_F z_G = \sum_{n=1}^{\infty} m_n z'_n \tag{24}$$

and thus, using Eq. (11c):

$$\frac{m_F}{4h} \sum_{n=1}^{\infty} \overline{\eta}_n^2 \frac{\left(\xi_n^2 - 1\right)}{\xi_n^2} = \sum_{n=1}^{\infty} m_n z'_n. \tag{25}$$

[2] In the particular case of a one-dimensional lateral harmonic excitation $x_c(t) = X_0 \cos \Omega t$ (as in Eq. (1)), Eqs. (7) and (21) must coincide, yielding:

$$x_n = \frac{\Omega^2 x_c(t)}{\omega_n^2 - \Omega^2}$$

which is indeed the steady-state solution of the second-order harmonic equation governing the motion of the n-th sloshing mass for this particular case (see Section 5.2.1 of [14]).

A sufficient condition for (25) to hold is:

$$\frac{m_F}{4h} \overline{\eta}_n^2 \frac{\left(\xi_n^2 - 1\right)}{\xi_n^2} = m_n z'_n. \tag{26}$$

By using the expressions of $\overline{\eta}_n$, m_n/m_F and ω_n given, respectively, in Eqs. (21), (13) and (12), z'_n can be written as:

$$z'_n = \frac{\omega_n^2}{2g}(x_n^2 + y_n^2) = \frac{1}{2l_n}(x_n^2 + y_n^2), \tag{27}$$

where the physical meaning of the parameter

$$l_n = \frac{g}{\omega_n^2} \tag{28}$$

will be clarified in Section 4.1 (see Eq. (29) therein). Equation (27) shows that, to replicate the behavior of the CoM of the continuum model described in Section 2, the n-th sloshing mass of the discrete model must move on the paraboloidal surface described by Eqs. (23) and (27). Accordingly, the MSD model has 2 degrees of freedom for each sloshing mode.

4 Pendulum model

4.1 Model parameters

The PEN model comprises a mass m_0 representing the portion of the liquid not involved in sloshing and a series of spherical pendulums representing the sloshing modes, each with mass m_n and length l_n (Fig. 4). Each mass m_n is restrained by a dashpot with damping coefficient c_n, representing the fluid viscosity, and the n-th pendulum pivot is placed at a height $h_n + l_n$ from the undisturbed CoM.

As for the MSD models, the parameters can be determined by imposing a number of equivalence conditions with the continuum system [14]. In particular, Eqs. (12), (13), and (17) still hold. Equating (12) with the natural frequency of a

simple pendulum (equal to $\sqrt{g/l_n}$) allows the length of the n-th pendulum to be computed as:

$$l_n = \frac{g}{\omega_n^2} = \frac{R}{\xi_n \tanh\left(\xi_n \frac{h}{R}\right)}. \tag{29}$$

The n-th sloshing mass is constrained to move on a sphere, so that its generalized coordinates (x_n, y_n, z_n) must satisfy the spherical constraint $x_n^2 + y_n^2 + z_n^2 = l_n^2$. For consistency with the notation commonly adopted in the literature on the PEN model, the position of the sloshing mass can alternatively be described using Euler angles (ϕ_{yn}, ϕ_{xn}) according to the yx convention, which does not exhibit singularities in the rest configuration.[3]

4.2 Sloshing-height formulation

In contrast to the MSD models, there is no universally accepted formulation of the sloshing height for the PEN model. For simplicity, especially in control-oriented studies, sloshing is often approximated using a single pendulum, which is assumed to remain perpendicular to the planar liquid free surface [37]. In this framework, the sloshing height can be inferred from the tangent of the pendulum angular displacement [20, 37]. Although intuitive, this approach reduces the model to a single sloshing mass and fails to preserve consistency with the continuum representation. Consequently, alternative formulations are proposed in the following.

4.2.1 Tangent-based Formulation

Since the pendulum rod is assumed to remain perpendicular to the liquid free surface, the angles ϕ_{y1} and ϕ_{x1} of the first sloshing mode define a plane that intersects the cylindrical container wall to form an ellipse. Since the container has radius R, if β is the so-called *sloshing angle*, namely the angle that the pendulum rod forms with the vertical axis, the sloshing height $\overline{\eta}$ can be computed as:

$$\overline{\eta} = R \tan \beta. \tag{30}$$

[3] A more intuitive approach uses Euler angles (ϕ_{zn}, ϕ_{yn}) following the zy convention, where ϕ_{zn} defines the oscillation plane about the z-axis and ϕ_{yn} describes the pendulum swing within that plane. However, this representation is singular at rest, when $\phi_{yn} = 0$, as ϕ_{zn} becomes undefined and the Jacobian mapping $(\dot{\phi}_{zn}, \dot{\phi}_{yn})$ to Cartesian velocities becomes rank-deficient [36]. To avoid this issue, elementary rotations about the z-axis should be avoided. The orientation parameterization adopted in this Section still presents singularities, but only outside the model's valid operating range.

Since the unit vector $\mathbf{n}$ aligned with the pendulum rod is given by:

$$\boldsymbol{n} = \mathbf{R}_y(\phi_{y1})\mathbf{R}_x(\phi_{x1}) \begin{bmatrix} 0 \\ 0 \\ -1 \end{bmatrix} = \begin{bmatrix} -\cos\phi_{x1} \sin\phi_{y1} \\ \sin\phi_{x1} \\ -\cos\phi_{x1} \cos\phi_{y1} \end{bmatrix}, \tag{31}$$

the sloshing angle is:

$$\beta = \arccos\left(|\, -\cos\phi_{x1} \cos\phi_{y1} \,|\right). \tag{32}$$

4.2.2 CoM conservation

An alternative formulation defines the sloshing height based on the CoM conservation between the continuum and the discrete model. Given the position of the pendulum mass in $Oxyz$:

$$\begin{aligned} \begin{bmatrix} x_n \\ y_n \\ z_n \end{bmatrix} &= l_n \boldsymbol{n} + \begin{bmatrix} 0 \\ 0 \\ h_n + l_n \end{bmatrix} = \\ &= \begin{bmatrix} -l_n(\sin\phi_{yn} \cos\phi_{xn}) \\ l_n(\sin\phi_{xn}) \\ h_n + l_n\left(1 - \cos\phi_{yn} \cos\phi_{xn}\right) \end{bmatrix}, \end{aligned} \tag{33}$$

the CoM conservation along the x and the y axes is obtained by substituting Eq. (33) in Eq. (21) and by using the expressions of m_n/m_F, ω_n and l_n given, respectively, in Eqs. (13), (12) and (29), yielding:

$$\overline{\eta}_n = \frac{2R}{\xi_n^2 - 1} \sqrt{\sin^2\phi_{yn} \cos^2\phi_{xn} + \sin^2\phi_{xn}}. \tag{34}$$

The conservation of the CoM along the z-direction (Fig. 4c) is obtained by substituting Eq. (33) into Eq. (22) and considering Eq. (16), namely:

$$z_G m_F = \sum_{n=1}^{\infty} m_n l_n (1 - \cos\phi_{yn} \cos\phi_{xn}), \tag{35}$$

which, recalling Eq. (11c), becomes:

$$\begin{aligned} \frac{m_F}{4h} \sum_{n=1}^{\infty} \overline{\eta}_n^2 \frac{\left(\xi_n^2 - 1\right)}{\xi_n^2} = \\ = \sum_{n=1}^{\infty} m_n l_n \left(1 - \cos\phi_{xn} \cos\phi_{yn}\right). \end{aligned} \tag{36}$$

A sufficient condition to satisfy Eq. (36) is:

$$\overline{\eta}_n^2 \frac{\left(\xi_n^2 - 1\right)}{4h\xi_n^2} m_F = m_n l_n \left(1 - \cos\phi_{xn} \cos\phi_{yn}\right). \tag{37}$$

By using the expressions of m_n/m_F, ω_n and l_n given, respectively, in Eqs. (13), (12) and (29), Eq. (37) provides:

$$\overline{\eta}_n = \frac{2R}{\xi_n^2 - 1}\sqrt{2\left(1 - \cos\phi_{xn}\cos\phi_{yn}\right)}. \tag{38}$$

As evident from Eqs. (34) and (38), the sloshing-height formulations, obtained by matching the CoM of the PEN model to that of the continuum model, yield different results depending on whether the radial or vertical direction is considered. This discrepancy indicates that the pendulum model, which constrains the sloshing mass to move on a spherical surface, cannot fully replicate the continuum-model behavior. Accordingly, if the formulation in Eq. (30) is also taken into account, there are three possible ways to evaluate the sloshing height in the PEN model. Their relative performance will be assessed in Section 7.

5 Qualitative comparison of the discrete models

5.1 Geometry and sloshing-height formulation

The PMSD and PEN models share the same expressions of m_n, ω_n and ζ_n. The main difference lies in the way the two models express the vertical coordinate of the sloshing masses: in the PMSD model sloshing masses slide on paraboloidal surfaces, whereas in the PEN model sloshing masses are constrained to move on spherical surfaces of radius l_n. Accordingly, the PMSD and PEN models provide different expressions for the vertical coordinate z_n of the n-th sloshing mass as a function of the generalized coordinates x_n and y_n (Figs. 5a, 5b):

$$z_n = h_n + \frac{1}{2l_n}(x_n^2 + y_n^2) = f_{PMSD}(x_n, y_n), \tag{39a}$$

$$z_n = h_n + l_n - \sqrt{l_n^2 - x_n^2 - y_n^2} = f_{PEN}(x_n, y_n). \tag{39b}$$

The expression of z_n from the LMSD model, i.e. $z_n = h_n = f_{LMSD}(x_n, y_n)$, represents the first-order approximation of both models near $(x_n, y_n) = (0, 0)$ (see Fig. 5c) since the first-order derivatives of f_{PMSD} and f_{PEN} are:

$$\frac{\partial f_{PMSD}}{\partial x_n} = \frac{1}{l_n}x_n, \quad \frac{\partial f_{PMSD}}{\partial y_n} = \frac{1}{l_n}y_n, \tag{40}$$

$$\begin{aligned}\frac{\partial f_{PEN}}{\partial x_n} &= \frac{x_n}{\sqrt{l_n^2 - x_n^2 - y_n^2}},\\ \frac{\partial f_{PEN}}{\partial y_n} &= \frac{y_n}{\sqrt{l_n^2 - x_n^2 - y_n^2}},\end{aligned} \tag{41}$$

and they are all zero near the container axis. The second-order derivatives of f_{PMSD} and f_{PEN} w.r.t. x_n and y_n, namely

$$\frac{\partial^2 f_{PMSD}}{\partial x_n^2} = \frac{1}{l_n}, \quad \frac{\partial^2 f_{PMSD}}{\partial x_n \partial y_n} = 0, \quad \frac{\partial^2 f_{PMSD}}{\partial y_n^2} = \frac{1}{l_n}, \tag{42}$$

$$\begin{aligned}\frac{\partial^2 f_{PEN}}{\partial x_n^2} &= \frac{l_n^2 - y_n^2}{\left(l_n^2 - x_n^2 - y_n^2\right)^{3/2}},\\ \frac{\partial^2 f_{PEN}}{\partial y_n^2} &= \frac{l_n^2 - x_n^2}{\left(l_n^2 - x_n^2 - y_n^2\right)^{3/2}},\\ \frac{\partial^2 f_{PEN}}{\partial x_n \partial y_n} &= \frac{x_n y_n}{\left(l_n^2 - x_n^2 - y_n^2\right)^{3/2}},\end{aligned} \tag{43}$$

also coincide in $(x_n, y_n) = (0, 0)$, which means that, for small oscillations of the liquid, the PMSD and PEN models coincide until the second-order approximation. However, they diverge as oscillations grow larger, and so do the corresponding sloshing-height estimations.

Table 1 summarizes the sloshing-height formulations proposed for both models, with the results from Eqs. (21), (30), (34) and (38) substituted into Eq. (9). As noted in Section 4.2.2 and emphasized by the check marks in Table 1, the PMSD model enforces the CoM conservation in both the radial (x, y) and vertical (z) directions. In contrast, the PEN model allows CoM conservation to be enforced in only one direction, either radial (PEN-rad) or vertical (PEN-vert), or in neither, as in the PEN-tan formulation. Additionally, the PEN-tan formulation only considers the first sloshing mode.

5.2 Lagrange terms

The EOMs describing the time evolution of the generalized coordinates (q_1, q_2), which represent (x_n, y_n) for the PMSD case and (ϕ_{yn}, ϕ_{xn}) for the PEN model, can be obtained by means of Lagrange Equations:

$$\frac{d}{dt}\left(\frac{\partial T}{\partial \dot{q}_i}\right) - \frac{\partial T}{\partial q_i} + \frac{\partial V}{\partial q_i} + \frac{\partial D}{\partial \dot{q}_i} = 0, \quad \text{for } i = 1, 2, \tag{44}$$

where

$$T = T_0 + \sum_{n=1}^{\infty} T_n, \quad D = \sum_{n=1}^{\infty} D_n, \quad V = V_0 + \sum_{n=1}^{\infty} V_n, \tag{45}$$

are the system kinetic energy, Rayleigh dissipation function, and potential energy, respectively. In particular, the terms with subscript 0 refer to the rigid mass m_0 and do not depend on the generalized coordinates (q_1, q_2), whereas the energy contributions with subscript n are associated with the n-th sloshing mass. Regardless of the adopted model (PMSD or PEN) and the motion type (SCARA or Tilting), the position

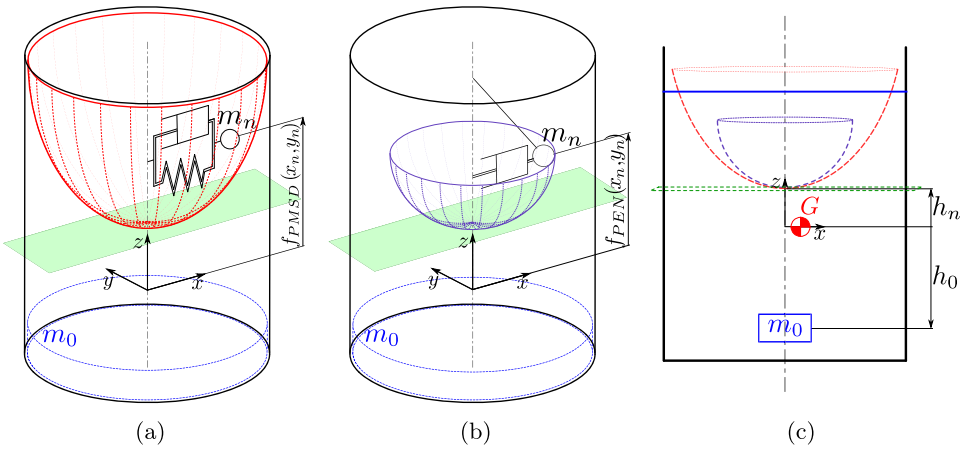

Fig. 5 Constraint surfaces: (**a**) PMSD model, (**b**) PEN model, (**c**) lateral view of the LMSD (in green), PMSD (in red) and PEN (in purple) models

Table 1 Sloshing-height formulations.

Sloshing-Height Formulation	x, y	z	Nomenclature
$\overline{\eta} = \sum_{n=1}^{\infty} \frac{2R\omega_n^2}{g(\xi_n^2 - 1)} \sqrt{x_n^2 + y_n^2}$	✓	✓	PMSD
$\overline{\eta} = R \tan \beta$	-	-	PEN-tan
$\overline{\eta} = \sum_{n=1}^{\infty} \frac{2R}{\xi_n^2 - 1} \sqrt{\sin^2 \phi_{yn} \cos^2 \phi_{xn} + \sin^2 \phi_{xn}}$	✓	-	PEN-rad
$\overline{\eta} = \sum_{n=1}^{\infty} \frac{2R}{\xi_n^2 - 1} \sqrt{2\left(1 - \cos \phi_{xn} \cos \phi_{yn}\right)}$	-	✓	PEN-vert

of the n-th sloshing mass in the inertial frame can be denoted as ${}^0\mathbf{s}_n = [s_{n,x}\ s_{n,y}\ s_{n,z}]^T$, and its velocity as ${}^0\dot{\mathbf{s}}_n$. The kinetic energy T_n of the n-th sloshing mass is thus:

$$T_n = \frac{1}{2} m_n \left\| {}^0\dot{\mathbf{s}}_n \right\|^2. \tag{46}$$

The dissipation function D_n accounts for the energy dissipation due to the relative motion of the n-th sloshing mass w.r.t. the container and so is:

$$D_n = \frac{1}{2} c_n \left(\dot{x}_n^2 + \dot{y}_n^2 + \dot{z}_n^2 \right). \tag{47}$$

Given the different expressions of z_n in Eqs. (39a) and (39b), the PMSD and PEN models provide different values of T_n and D_n, although sharing the same formulations. The potential energy V_n has distinct formulations in the two models, due to the presence of the spring in the PMSD model. More precisely, if the LMSD model is also considered, V_n is given by:

$$V_n = \begin{cases} V_g, \text{ PEN Model} & \text{(48a)} \\ V_g + V_e(\alpha, w), \text{ PMSD Model} & \text{(48b)} \\ V_e(1,\ 1), \text{ LMSD Model} & \text{(48c)} \end{cases}$$

where the gravitational potential energy is

$$V_g = m_n g s_{n,z}, \tag{49}$$

and the elastic potential energy V_e of the spring of order w is:

$$V_e(\alpha, w) = \frac{\alpha k_n}{2w R^{2w-2}} \left(x_n^2 + y_n^2 \right)^w. \tag{50}$$

Note that, when $w = \alpha = 1$, as in the LMSD model, the potential energy in (50) reduces to that of a standard linear spring, i.e.,

$$V_e(1,\ 1) = \frac{k_n}{2} \left(x_n^2 + y_n^2 \right).$$

The restoring force that counterbalances inertial effects is given by $[\partial V_n / \partial x_n, \partial V_n / \partial y_n]^T$. While a single contribution to the restoring force is present in the PEN and LMSD models, due to either gravity (PEN) or the spring (LMSD), the PMSD model comprises both terms. Interestingly, if the container does not tilt, the gravitational contribution V_g in the PMSD model is equal, up to an additive constant, to the elastic potential energy $V_e(1, 1)$ of the LMSD model. In fact, if z_c is the container elevation, z_n is taken from Eq. (39a), and l_n from Eq. (29), then

$$V_g = m_n g s_{n,z} = m_n g \left[z_c + \frac{h}{2} + h_n + \frac{x_n^2 + y_n^2}{2l_n} \right] =$$
$$= m_n g \left(z_c + \frac{h}{2} + h_n \right) + \frac{m_n g}{2l_n}(x_n^2 + y_n^2) =$$
$$= \text{Const} + \frac{m_n g}{2l_n}(x_n^2 + y_n^2). \tag{51}$$

Since, from Eqs. (12) and (29):

$$k_n = m_n \frac{g}{l_n}, \tag{52}$$

it follows

$$V_g = \text{Const} + \frac{k_n}{2}(x_n^2 + y_n^2) = \text{Const} + V_e(1,1). \tag{53}$$

This consideration suggests that, in the PMSD model, the nonlinear elastic term is not strictly necessary, leading to the definition of a simplified PMD model (without spring), in which it is simply assumed that $\alpha = 0$.

6 Equations of motion

To extend the discrete models presented in [18, 32] and account for an additional container rotation, two motion types are considered:

- SCARA motion: a $3D$ translation is combined with an instantaneous rotation about a vertical axis, so that the container linear and angular accelerations are $\ddot{\mathbf{S}}_c = [\ddot{x}_c \;\; \ddot{y}_c \;\; \ddot{z}_c]^T$, $\dot{\boldsymbol{\Omega}}_c = [0 \;\; 0 \;\; \ddot{\theta}_c]^T$;
- tilting motion: a $3D$ translation is combined with an instantaneous tilting rotation about an axis that remains parallel to the y-axis, so that the container linear and angular accelerations are $\ddot{\mathbf{S}}_c = [\ddot{x}_c \;\; \ddot{y}_c \;\; \ddot{z}_c]^T$, $\dot{\boldsymbol{\Omega}}_c = [0 \;\; \ddot{\psi}_c \;\; 0]^T$,

where x_c, y_c, z_c, θ_c and ψ_c are coordinates that represent the translational and rotational displacement of the container w.r.t. the fixed frame. In particular, $\mathbf{S}_c$ is the position vector of the centerpoint O_c of the container base, whereas θ_c and ψ_c are the container rotations about the Z and the Y axis, respectively. The EOMs for the two models presented in Sections 3 and 4 will be derived by means of the Lagrange Equations, exploiting the results of Section 5.2.

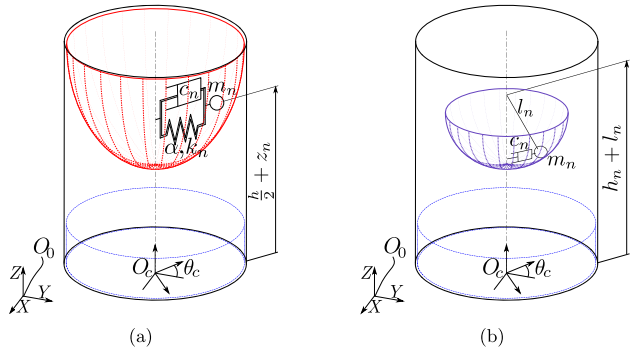

Fig. 6 Schematics of the container under SCARA motion: (**a**) PMSD model; (**b**) PEN model

6.1 SCARA motion

6.1.1 PMSD Model

The position ${}^0\mathbf{s}_n$ of the n-th sloshing mass is (Fig. 6a):

$${}^0\mathbf{s}_n = \begin{bmatrix} x_c \\ y_c \\ z_c \end{bmatrix} + \mathbf{R}_z(\theta_c) \begin{bmatrix} x_n \\ y_n \\ \frac{h}{2} + z_n \end{bmatrix} =$$
$$= \begin{bmatrix} x_c + x_n \cos\theta_c - y_n \sin\theta_c \\ y_c + x_n \sin\theta_c + y_n \cos\theta_c \\ z_c + \frac{h}{2} + h_n + \dfrac{1}{2l_n}(x_n^2 + y_n^2) \end{bmatrix}, \tag{54}$$

where $\mathbf{R}_z$ is the rotation matrix expressing an elementary rotation about the vertical z-axis. By adopting Eq. (44) for $(q_1, q_2) = (x_n, y_n)$, and substituting the expressions of ${}^0\mathbf{s}_n$ and its time derivative ${}^0\dot{\mathbf{s}}_n$ computed from Eq. (54) into T_n, D_n, and V_n (see Eqs. (46), (47), (48a)), we obtain the following EOMs:

$$\begin{cases} \left(1 + \frac{1}{l_n^2}x_n^2\right)\ddot{x}_n + \frac{1}{l_n^2}x_n y_n \ddot{y}_n = -\frac{1}{l_n^2}(\dot{x}_n^2 + \dot{y}_n^2)x_n + \\ +(2\dot{\theta}_c \dot{y}_n + \dot{\theta}_c^2 x_n + \ddot{\theta}_c y_n) + \\ -\omega_n^2 x_n \left[1 + \frac{\alpha}{R^{2w-2}}(x_n^2 + y_n^2)^{w-1}\right] + \\ -2\omega_n \zeta_n [\dot{x}_n + \frac{1}{l_n^2}(x_n \dot{x}_n + y_n \dot{y}_n)x_n] + \\ -\ddot{x}_c \cos\theta_c - \ddot{y}_c \sin\theta_c - \ddot{z}_c \frac{1}{l_n} x_n \\ \left(1 + \frac{1}{l_n^2}y_n^2\right)\ddot{y}_n + \frac{1}{l_n^2}x_n y_n \ddot{x}_n = -\frac{1}{l_n^2}(\dot{x}_n^2 + \dot{y}_n^2)y_n + \\ +(-2\dot{\theta}_c \dot{x}_n + \dot{\theta}_c^2 y_n - \ddot{\theta}_c x_n) + \\ -\omega_n^2 y_n \left[1 + \frac{\alpha}{R^{2w-2}}(x_n^2 + y_n^2)^{w-1}\right] + \\ -2\omega_n \zeta_n [\dot{y}_n + \frac{1}{l_n^2}(x_n \dot{x}_n + y_n \dot{y}_n)y_n] + \\ +\ddot{x}_c \sin\theta_c - \ddot{y}_c \cos\theta_c - \ddot{z}_c \frac{1}{l_n} y_n \end{cases} \tag{55}$$

6.1.2 Pendulum Model

Similarly, the PEN-model EOMs can be obtained from Eq. (44). The position vector ${}^0\mathbf{s}_n$ of the n-th sloshing mass, as modeled through the spherical angles, becomes (Fig. 6b)

$$
\begin{aligned}
{}^0\mathbf{s}_n &= \begin{bmatrix} x_c \\ y_c \\ z_c \end{bmatrix} + \mathbf{R}_z(\theta_c) \begin{bmatrix} 0 \\ 0 \\ h_n + l_n \end{bmatrix} + \\
&+ \mathbf{R}_z(\theta_c)\mathbf{R}_y(\phi_{yn})\mathbf{R}_x(\phi_{xn}) \begin{bmatrix} 0 \\ 0 \\ -l_n \end{bmatrix} = \\
&= \begin{bmatrix} x_c - l_n \left(\sin\phi_{xn}\ \sin\theta_c + \cos\phi_{xn}\ \cos\theta_c \sin\phi_{yn}\right) \\ y_c + l_n \left(\sin\phi_{xn} \cos\theta_c - \cos\phi_{xn} \sin\theta_c \sin\phi_{yn}\right) \\ z_c + h_n + l_n \left(1 - \cos\phi_{xn} \cos\phi_{yn}\right) \end{bmatrix},
\end{aligned} \tag{56}
$$

with $\mathbf{R}_x$, $\mathbf{R}_y$, $\mathbf{R}_z$ being elementary rotations about axes x, y and z, respectively.

Substituting Eq. (56) and its time derivative into Eqs. (46), (47), and (48a), and substituting these results into Eq. (44) with $(q_1, q_2) = (\phi_{xn}, \phi_{yn})$, yields:

$$
\begin{cases}
\ddot{\phi}_{yn} \cos\phi_{xn} = -2\omega_n\zeta_n \cos\phi_{xn}\dot{\phi}_{yn} + \\
\quad + \frac{1}{l_n} \cos\phi_{yn}(\cos\theta_c\ddot{x}_c + \sin\theta_c\ddot{y}_c) + \\
\quad - \frac{1}{l_n} \sin\phi_{yn}(g + \ddot{z}_c) + 2\sin\phi_{xn}\dot{\phi}_{yn}\dot{\phi}_{xn} + \\
\quad - \cos\phi_{yn} \sin\phi_{xn}\ddot{\theta}_c + \\
\quad + \cos\phi_{xn} \cos\phi_{yn} \left(\sin\phi_{yn}\dot{\theta}_0^2 - 2\dot{\theta}_c\dot{\phi}_{xn}\right) \\
\\
\ddot{\phi}_{xn} = -2\omega_n\zeta_n\dot{\phi}_{xn} + \frac{1}{l_n}(\cos\phi_{xn} \sin\theta_c + \\
\quad - \sin\phi_{xn} \cos\theta_c \sin\phi_{yn})\ddot{x}_c + \\
\quad - \frac{1}{l_n}(\sin\phi_{xn} \sin\phi_{yn} \sin\theta_c + \cos\theta_c \cos\phi_{xn})\ddot{y}_c + \\
\quad - \frac{1}{l_n} \cos\phi_{yn} \sin\phi_{xn}(g + \ddot{z}_c) + \sin\phi_{yn}\ddot{\theta}_c + \\
\quad - \cos\phi_{xn} \sin\phi_{xn}\dot{\phi}_{yn}^2 + \\
\quad + \cos\phi_{xn} \cos^2\phi_{yn} \sin\phi_{xn}\dot{\theta}_c^2 + \\
\quad + 2\cos^2\phi_{xn} \cos\phi_{yn}\dot{\theta}_c\dot{\phi}_{yn}
\end{cases} \tag{57}
$$

6.2 Tilting motion

6.2.1 PMSD Model

The position vector ${}^0\mathbf{s}_n$ of the n-th sloshing mass is in this case (Fig. 7a):

$$
\begin{aligned}
{}^0\mathbf{s}_n &= \begin{bmatrix} x_c \\ y_c \\ z_c \end{bmatrix} + \mathbf{R}_y(\psi_c) \begin{bmatrix} x_n \\ y_n \\ \frac{h}{2} + z_n \end{bmatrix} = \\
&= \begin{bmatrix} x_c + x_n \cos\psi_c + \left[\frac{h}{2} + h_n + \frac{1}{2l_n}(x_n^2 + y_n^2)\right] \sin\psi_c \\ y_c + y_n \\ z_c - x_n \sin\psi_c + \left[\frac{h}{2} + h_n + \frac{1}{2l_n}(x_n^2 + y_n^2)\right] \cos\psi_c \end{bmatrix}.
\end{aligned} \tag{58}
$$

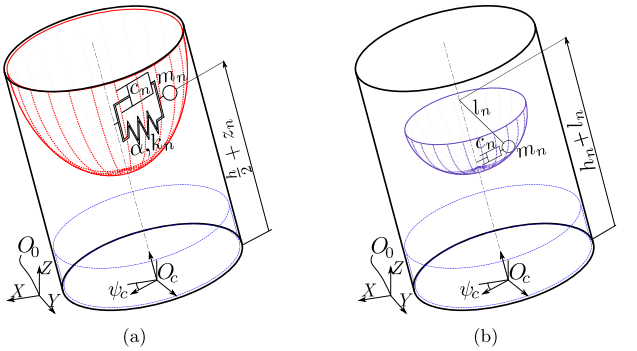

Fig. 7 Schematics of the container under tilting motion: (**a**) PMSD model, (**b**) PEN model

Equation (44) with $(q_1, q_2) = (x_n, y_n)$ and T_n, D_n, and V_n obtained from Eqs. (46, 47, (48b)) yields:

$$
\begin{cases}
\left(1 + \frac{1}{l_n^2}x_n^2\right)\ddot{x}_n + \frac{1}{l_n^2}x_n y_n \ddot{y}_n = -\frac{1}{l_n^2}(\dot{x}_n^2 + \dot{y}_n^2)x_n + \\
\quad + \left[-2\frac{1}{l_n}y_n\dot{y}_n\dot{\psi}_c + (x_n + H_n\frac{1}{l_n}x_n)\dot{\psi}_c^2 - (H_n - \frac{1}{l_n}x_n^2)\ddot{\psi}_c\right] + \\
\quad - \omega_n^2 x_n \left[\cos\psi_c + \frac{\alpha}{R^{2w-2}}(x_n^2 + y_n^2)^{w-1}\right] + \\
\quad - 2\omega_n\zeta_n[\dot{x}_n + \frac{1}{l_n^2}(x_n\dot{x}_n + y_n\dot{y}_n)x_n] + \\
\quad - (\ddot{x}_c \cos\psi_c - \ddot{z}_c \sin\psi_c) - (\ddot{x}_c \sin\psi_c + \\
\quad + \ddot{z}_c \cos\psi_c)\frac{1}{l_n}x_n + g\sin\psi_c \\
\\
\left(1 + \frac{1}{l_n^2}y_n^2\right)\ddot{y}_n + \frac{1}{l_n^2}x_n y_n \ddot{x}_n = -\frac{1}{l_n^2}(\dot{x}_n^2 + \dot{y}_n^2)y_n + \\
\quad + \left[2\frac{1}{l_n}y_n\dot{x}_n\dot{\psi}_c + H_n\frac{1}{l_n}y_n\dot{\psi}_c^2 + \frac{1}{l_n}x_n y_n\ddot{\psi}_c\right] + \\
\quad - \omega_n^2 y_n \left[\cos\psi_c + \frac{\alpha}{R^{2w-2}}(x_n^2 + y_n^2)^{w-1}\right] + \\
\quad - 2\omega_n\zeta_n[\dot{y}_n + \frac{1}{l_n^2}(x_n\dot{x}_n + y_n\dot{y}_n)y_n] + \\
\quad - \ddot{y}_c - (\ddot{x}_c \sin\psi_c + \ddot{z}_c \cos\psi_c)\frac{1}{l_n}y_n
\end{cases} \tag{59}
$$

where

$$
H_n = \frac{h}{2} + h_n + \frac{1}{2l_n}(x_n^2 + y_n^2). \tag{60}
$$

6.2.2 Pendulum Model

The position vector ${}^0\mathbf{s}_n$ of the n-th pendulum mass w.r.t. the fixed frame is (Fig. 7b):

$$
\begin{aligned}
{}^0\mathbf{s}_n &= \begin{bmatrix} x_c \\ y_c \\ z_c \end{bmatrix} + \mathbf{R}_y(\psi_c) \begin{bmatrix} 0 \\ 0 \\ h_n + l_n \end{bmatrix} + \\
&+ \mathbf{R}_y(\psi_c)\mathbf{R}_y(\phi_{yn})\mathbf{R}_x(\phi_{xn}) \begin{bmatrix} 0 \\ 0 \\ -l_n \end{bmatrix} = \\
&= \begin{bmatrix} x_c - l_n \cos\phi_{xn} \sin\left(\psi_c + \phi_{yn}\right) + (h_n + l_n)\sin\psi_c \\ y_c + l_n \sin\phi_{xn} \\ z_c - l_n \cos\phi_{xn} \cos\left(\psi_c + \phi_{yn}\right) + (h_n + l_n)\cos\psi_c \end{bmatrix}.
\end{aligned} \tag{61}
$$

Substituting Eq. (61) into Eqs. (46), (47), and (48a) and its time derivative, and using these results in Eq. (44) with $(q_1, q_2) = (\phi_{xn}, \phi_{yn})$, yields:

$$
\begin{cases}
\ddot{\phi}_{yn}\cos\phi_{xn} = -2\omega_n\zeta_n\cos\phi_{xn}\dot{\phi}_{yn} + \frac{1}{l_n}\cos(\psi_c+\phi_{yn})\ddot{x}_c + \\
\quad -\frac{1}{l_n}\sin(\psi_c+\phi_{yn})(g+\ddot{z}_c) + 2\sin\phi_{xn}\dot{\phi}_{xn}(\dot{\psi}_c+\dot{\phi}_{yn}) + \\
\quad -\frac{1}{l_n}\left(l_n\cos\phi_{xn} - (h_n+l_n)\cos\phi_{yn}\right)\ddot{\psi}_c + \\
\quad +\frac{(h_n+l_n)}{l_n}\sin\phi_{yn}\dot{\psi}_c^2 \\
\\
\ddot{\phi}_{xn} = -2\omega_n\zeta_n\dot{\phi}_{xn} - \frac{1}{l_n}\sin\phi_{xn}\sin(\psi_c+\phi_{yn})\ddot{x}_c + \\
\quad -\frac{1}{l_n}\cos\phi_{xn}\ddot{y}_c + \\
\quad -\frac{1}{l_n}\sin\phi_{xn}\cos(\psi_c+\phi_{yn})(g+\ddot{z}_c) + \\
\quad -\frac{(h_n+l_n)}{l_n}\sin\phi_{yn}\sin\phi_{xn}\ddot{\psi}_c + \\
\quad -\frac{1}{l_n}\sin\phi_{xn}\left(l_n\cos\phi_{xn} - (h_n+l_n)\cos\phi_{yn}\right)\dot{\psi}_c^2 + \\
\quad -\sin\phi_{xn}\cos\phi_{xn}\dot{\phi}_{yn}^2 - 2\sin\phi_{xn}\cos\phi_{xn}\dot{\phi}_{yn}\dot{\psi}_c
\end{cases}
\tag{62}
$$

7 Experimental validation

This Section presents the results of an extensive experimental campaign performed to compare the accuracy achieved by the different formulations presented in Sections 3 and 4 under SCARA and tilting motions.

The experiments were conducted for several values of the ratio h/R, which is the dominant geometric parameter governing the liquid dynamics (see Sections 3.2 and 4.1). Specifically, a cylindrical container of radius $R = 49$mm was filled with colored water at static heights ranging from 30mm to 78mm, corresponding to h/R values in the range [0.6, 1.6]. For brevity, only the results for $h = 30$mm, 49mm, and 78mm, corresponding respectively to $h/R = 0.6$, 1, and 1.6, are reported in the following. Smaller values of h/R could not be explored because, under the tested dynamics, the resulting maximum sloshing height would become comparable to R, causing the liquid free surface to come into contact with the container bottom and thereby invalidating the underlying models. For the selected values of h/R, the corresponding model parameters (including up to three sloshing masses), as introduced in Sections 3.2 and 4.1, are summarized in Table 2.

The trajectories were performed by an industrial robot (Comau Smart-Six), whose end-effector was equipped with two GoPro Hero8 cameras to record the liquid behavior during motion. The cameras were placed with an angular offset of 90° to help the detection of the liquid peak, which can occur wherever on the container wall (see Fig. 8). The experimental sloshing heights were extracted from the videos recorded by the cameras using the video-processing algorithm described in [32], adapted to a two-camera setup to enable a more robust identification of the liquid peak on the container surface.

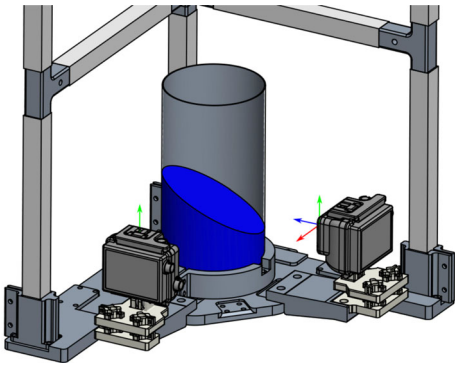

Fig. 8 Setup adopted for the image processing analysis

All datasets collected during the experiments are freely accessible to the scientific community in the public repository [33].

7.1 Geometrical paths and motion laws

Several paths, representative of typical industrial pick-and-place operations, were tested under different dynamic motion laws, yielding consistent results across all trajectories. For brevity, we report only the results for six paths exhibiting the highest dynamics while maintaining the liquid motion in a weakly nonlinear regime, with container accelerations up to 7.2m/s^2 and 11.0rad/s^2, as these motions are considered the most meaningful and representative of the overall validation campaign.

The paths for SCARA motion are:

- an eight-shaped path on the xy plane with an additional vertical excursion, combined with a rotation about the container axis (Se-motion);
- a rotation about a vertical axis that is at a certain distance d from the container axis, performed twice in succession, with the addition of an excitation along the vertical direction (Sc-motion);
- a rotation about a vertical axis at a distance d from the container axis with the addition of a translation along the x and z axes (Sg-motion).

The resulting paths are shown using solid lines in Fig. 9.

As far as the tilting trajectories are concerned, the same translational paths shown in Figs. 9a,b,c are used, but they are combined with a tilting excitation ψ_c about an axis that remains parallel to the y-axis throughout the motion. The resulting motions are denoted as Te, Tc, Tg, and they are depicted in Figs. 10a,b,c.

Table 3 contains the analytical expressions of the 4D paths followed by the container. The position and angular coordinates $x_c, y_c, z_c, \theta_c, \psi_c$ are written as functions of a path parameter σ, whose motion law $\sigma(t), \dot{\sigma}(t), \ddot{\sigma}(t)$ gives the

Table 2 Parameters of the LMSD, PMSD and PEN models, as introduced in Sections 3.2 and 4.1

h/R	R [mm]	h [mm]	m_F [kg]	n	ω_n [rad/s]	l_n [mm]	m_n [kg]	h_n [mm]	ζ_n
0.6	49	30	0.2259	1	17.2772	32.9	0.1358	-6.6	0.0064
				2	32.6174	9.2	0.0050	5.8	0.0051
				3	41.3319	5.7	0.0012	9.3	0.0050
1.0	49	49	0.3689	1	18.7189	28.0	0.1595	-0.8	0.0055
				2	32.6644	9.2	0.0050	15.3	0.0050
				3	41.3331	5.7	0.0012	18.8	0.0050
1.6	49	78	0.5873	1	19.1414	26.8	0.1667	12.5	0.0052
				2	32.6651	9.2	0.0050	29.8	0.0050
				3	41.3331	5.7	0.0012	33.3	0.0050

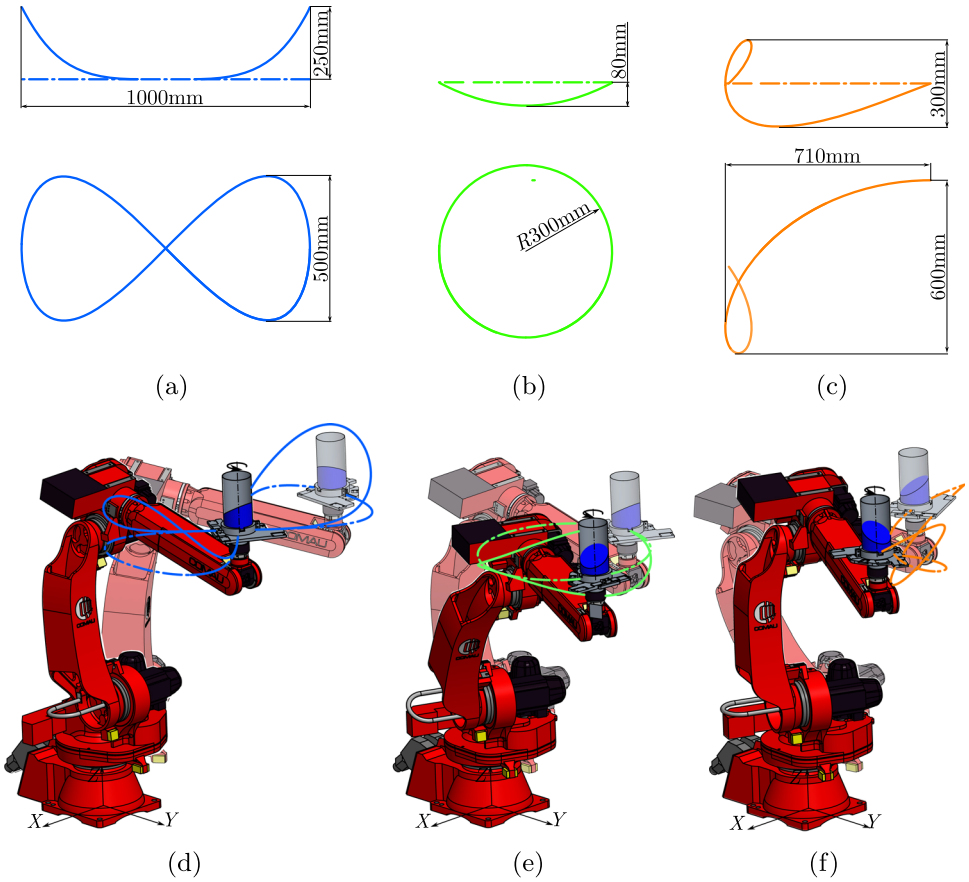

Fig. 9 The SCARA paths followed by the robot during experimental validation. (**a**), (**b**), (**c**): Se, Sc, Sg paths of the centerpoint O_c of the container base, respectively (the top image is the lateral view, whereas the bottom image is the view from the top). (**d**), (**e**), (**f**): overall Se, Sc, Sg motions of the container, respectively

container trajectory as a function of time[4]. The trend of the second time derivative $\ddot{\sigma}(t)$ is a modified trapezoidal motion law with 6 segments, whose free parameter is the trajectory time T_e (see Fig. 11). The maximum accelerations reached in each motion are presented in Table 4.

[4] The acceleration $\ddot{\mathbf{S}}_c$ can be written as $\ddot{\mathbf{S}}_c(\sigma, \dot{\sigma}, \ddot{\sigma}) = \mathbf{S}_0''(\sigma)\dot{\sigma}^2 + \mathbf{S}_0'(\sigma)\ddot{\sigma}$, where $()' = \partial()/\partial\sigma$ denotes the derivative w.r.t. the path parameter σ.

7.2 Accuracy indices

Two types of accuracy indices are defined to compare the proposed sloshing-height formulations against the experimental data. The first index ϵ is the percentage error between the model (subscript mod) and the experimental (subscript exp) maxima detected during motion, namely:

$$\epsilon = \frac{\overline{\eta}_{max,mod} - \overline{\eta}_{max,exp}}{\overline{\eta}_{max,exp}} \times 100\%, \quad t \in [0, T_e]\,. \tag{63}$$

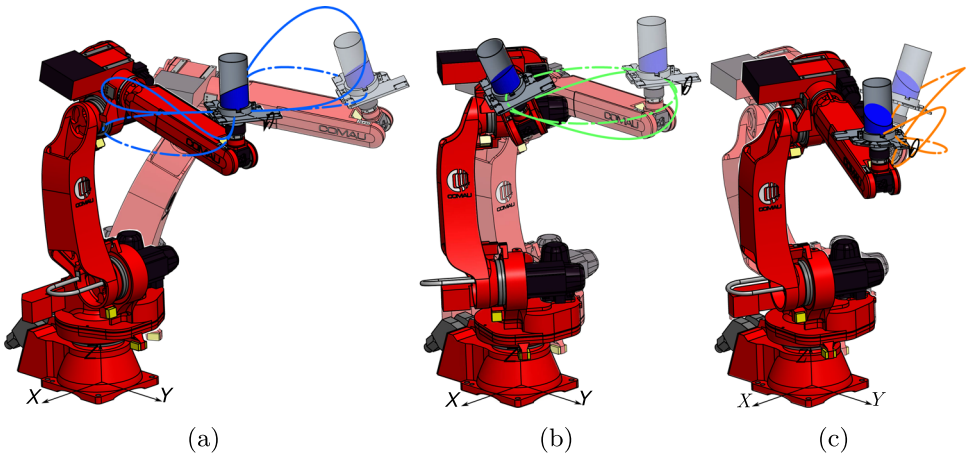

Fig. 10 The tilting motions followed by the robot during experiments: (**a**) Te-motion paths, (**b**) Tc-motion paths, (**c**) Tg-motion paths

The second index, λ, is the integral mean error between the model and the experimental trends, analyzed during the rest phase between T_e and $1.5T_e$, normalized with the mean experimental value during motion[5], i.e.:

$$\lambda = \frac{\int_{T_e}^{1,5T_e} \left[\overline{\eta}_{mod} - \overline{\eta}_{exp}(t)\right] dt}{\int_0^{T_e} \overline{\eta}_{exp}(t)\, dt} \frac{T_e}{0,5T_e} \times 100\%. \tag{64}$$

To facilitate the interpretation of the accuracy indices ϵ and λ, two representative time histories of the sloshing height $\overline{\eta}(t)$ are reported in Fig. 12, comparing the experimental measurements with the corresponding PMSD (Fig. 12a) and PEN model (Fig.12b) predictions.

In the PMSD model, the accuracy indices are functions of the spring parameters α and w, as well as of the number N of sloshing masses. In the PEN-model, the accuracy indices related to the PEN-rad and PEN-vert formulations only depend on N, whereas the PEN-tan formulation has no parameters, since it only considers one sloshing mode (see Table 1). The complete set of time histories of $\overline{\eta}_{exp}(t)$ and $\overline{\eta}_{mod}(t)$ for all considered models and for multiple values of α, w, and N is available in a public repository [33].

In the following Sections, ϵ and λ will be used to find the optimal value (if any) of the aforementioned parameters, and to compare the different sloshing models and sloshing-height formulations.

7.3 Quantitative comparison of the discrete models

7.3.1 PMSD Model

In this subsection, PMSD-based predictions of the sloshing height (Section 3.3) are compared with experimental data

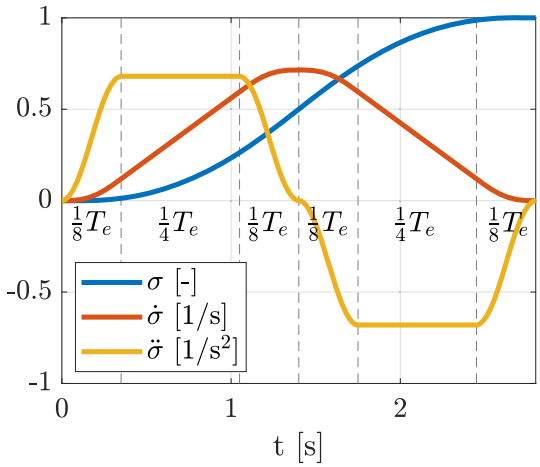

Fig. 11 Sample trends of $\sigma, \dot{\sigma}, \ddot{\sigma}$ for $T_e = 2.8$s

using the accuracy indices ϵ and λ. Results are reported for up to $N = 3$ sloshing masses. The model parameters α and w are varied over $\alpha \in [0,\ 1.5]$, with $w \in \{1, 2, 3\}$ and $N \in \{1, 2, 3\}$. No significant differences are observed among the three considered values of the fill ratio h/R. Figures 13a and 13b show $\epsilon(\alpha, w)$ and $\lambda(\alpha, w)$ for the Se, Sc, Sg, Te, Tc, Tg motions in the case $h/R = 1.6$. In each plot, blue, red, and yellow curves correspond to $w = 1$, $w = 2$, and $w = 3$, respectively; for each color (and hence for each nonlinear-spring power w), the solid line represents results for $N = 1$, the dashed line for $N = 2$, and the dotted line for $N = 3$. The figures corresponding to $h/R = 0.6$ and $h/R = 1$ are reported in Appendix A.2.1. For brevity, only the trends for $h/R = 1.6$ are discussed in the following. The numerical values, obtained with the PMSD model when $\alpha = 0$, are reported in Tables 5 and 6.

A larger number of sloshing masses consistently leads to a higher value of ϵ, thereby increasing the likelihood of overestimating the maximum sloshing height. However, while the rise in ϵ is significant when N increases from 1 to 2, it

[5] Normalization is performed using the mean experimental value between 0 and T_e, rather than between T_e and $1.5T_e$, because the former is larger and less affected by measurement errors, thus less likely to distort numerical results.

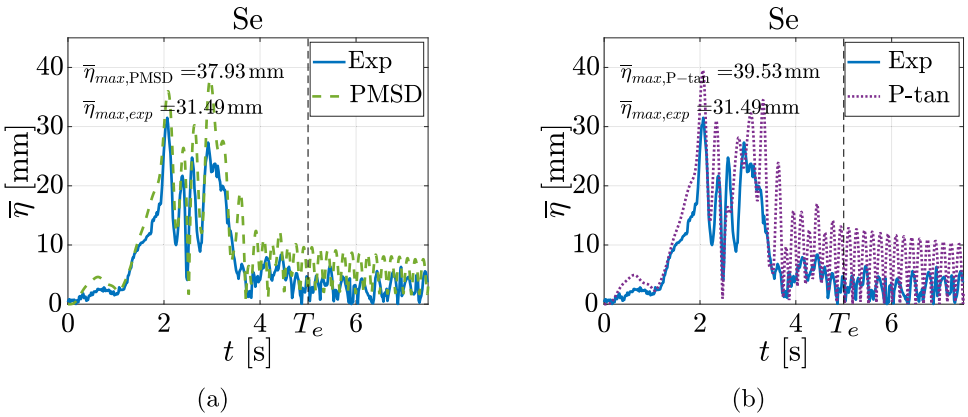

Fig. 12 Representative comparison of the PMSD and PEN model predictions against the experimental sloshing height for the Se motion in the case $h/R = 1.6$: results are obtained with the PMSD model using $\alpha = 0.5$, $w = 3$ and $N = 3$ (**a**), and with the PEN model employing the tangent-based formulation (PEN–tan) (**b**)

becomes much smaller from 2 to 3 (and it would be nearly negligible for higher values of N). In contrast, the number of sloshing masses has a minimal effect on λ, which characterizes residual oscillations.

For a given number of sloshing masses N, $\alpha = 0$ yields the highest values of ϵ and λ within the interval $\alpha \in [0, 1.5]$. These values are, in most cases, positive, thereby ensuring an overestimation of the sloshing height. Furthermore, choosing $\alpha = 0$ renders ϵ and λ independent of w. This is because $\alpha = 0$ removes the spring element from the model, thus reducing the restoring force and allowing for larger (modeled) oscillations. The resulting simplified system, composed solely of a mass and a damper, is referred to here as the Paraboloidal Mass-Damper (PMD) model.

When a conservative overestimation of liquid sloshing is desirable, as in trajectory-planning optimizations for indus-

Table 3 Paths followed by the container, with $d = 0.3$m, $a = 0.5$m, $b = 1$m and $\sigma \in [0, 1]$.

$\ddot{\mathbf{S}}_c = [\ddot{x}_c \;\; \ddot{y}_c \;\; \ddot{z}_c]^T$, $\dot{\boldsymbol{\Omega}}_c = [0 \;\; 0 \;\; \ddot{\theta}_c]^T$		
Se-motion	Sc-motion	Sg-motion
$x_c(\sigma) = a\cos(2\pi\sigma + \frac{\pi}{2})$	$x_c(\sigma) = d\cos(\theta_c(\sigma)) - d$	$x_c(\sigma) = d\cos(\theta_c(\sigma)) + b\sigma - d$
$y_c(\sigma) = -\frac{a}{2}\sin(4\pi\sigma + \pi)$	$y_c(\sigma) = -d\sin(\theta_c(\sigma))$	$y_c(\sigma) = -d\sin(\theta_c(\sigma))$
$z_c(\sigma) = \frac{y_c^2(\sigma) - x_c^2(\sigma)}{b^2}$	$z_c(\sigma) = \frac{x_c^2(\sigma) - (y_c(\sigma) + d)^2}{b^2} - \frac{d^2}{b^2}$	$z_c(\sigma) = \frac{d}{2}\sin\left(\frac{4}{3}\theta_c(\sigma)\right)$
$\theta_c(\sigma) = 5\pi\sigma$	$\theta_c(\sigma) = 4\pi\sigma$	$\theta_c(\sigma) = \frac{3}{2}\pi\sigma$
$\ddot{\mathbf{S}}_c = [\ddot{x}_c \;\; \ddot{y}_c \;\; \ddot{z}_c]^T$, $\dot{\boldsymbol{\Omega}}_c = [0 \;\; \ddot{\psi}_c \;\; 0]^T$		
Te-motion	Tc-motion	Tg-motion
$x_c(\sigma) = a\cos(2\pi\sigma + \frac{\pi}{2})$	$x_c(\sigma) = d\cos(4\pi\sigma) - d$	$x_c(\sigma) = d\cos\left(\frac{3}{2}\pi\sigma\right) + b\sigma - d$
$y_c(\sigma) = -\frac{a}{2}\sin(4\pi\sigma + \pi)$	$y_c(\sigma) = -d\sin(4\pi\sigma)$	$y_c(\sigma) = -d\sin\left(\frac{3}{2}\pi\sigma\right)$
$z_c(\sigma) = \frac{y_c^2(\sigma) - x_c^2(\sigma)}{b^2}$	$z_c(\sigma) = \frac{x_c^2(\sigma) - (y_c(\sigma) + d)^2}{b^2} - \frac{d^2}{b^2}$	$z_c(\sigma) = \frac{d}{2}\sin(2\pi\sigma)$
$\psi_c(\sigma) = -\frac{\pi}{6}\sin(2\pi\sigma)$	$\psi_c(\sigma) = -\frac{\pi}{6}\sin(2\pi\sigma)$	$\psi_c(\sigma) = \frac{\pi}{6}\sin(2\pi\sigma)$

Table 4 Maximum linear and angular accelerations reached during the different motions

Motion Type	$\lVert\ddot{\mathbf{S}}_c\rVert_{max}$ [m/s^2]	$\lvert\ddot{\theta}_c\rvert_{max}$ [rad/s^2]	$\lvert\ddot{\psi}_c\rvert_{max}$ [rad/s^2]	T_e[s]
Se	≈ 7.2	≈ 3.4	-	5.0
Sc	≈ 5.4	≈ 1.7	-	6.3
Sg	≈ 4.0	≈ 3.2	-	2.8
Te	≈ 5.0	-	≈ 8.7	6.0
Tc	≈ 5.1	-	≈ 7.4	6.5
Tg	≈ 5.0	-	≈ 11.0	2.5

trial applications, the aforementioned observations support the use of $\alpha = 0$ and $N = 2$ or 3, which produces the highest values of ϵ and λ among the tested formulations. Even in this conservative configuration, the PMD model maintains acceptable accuracy, with ϵ remaining below $\sim 20\%$ and λ below $\sim 50\%$, in all cases. The superior capability of discrete models to capture liquid dynamics during motion, as opposed to static conditions, has already been noted in the literature, e.g., in [25].

7.3.2 PEN Model

In this Subsection, the three sloshing-height formulations presented in Section 4.2 for the pendulum model are compared against experimental data. Up to $N = 3$ sloshing masses are considered for the method that enforces CoM equivalence with the continuum model, whereas only the first mode is analyzed for the tangent-based formulation.

Even for the PEN model, no significant differences are observed across the three selected values of the h/R ratio. Results for the two accuracy indices ϵ and λ are summarized in Tables 7 and 8 for the case $h/R = 1.6$. The tables corresponding to $h/R = 0.6$ and $h/R = 1$ are reported in Appendix A.2.2.

Table 7 shows that both the PEN-rad and PEN-vert formulations systematically underestimate the sloshing height, with the vertical formulation with three sloshing masses performing better, although it still significantly underestimates the sloshing height, with $\epsilon_{\text{PEN}-\text{vert N3}}$ ranging from -25.16% to -0.70%. On the contrary, the tangent-based formulation (PEN-tan), which includes only a single sloshing mass, consistently overestimates the sloshing height, with $\epsilon_{\text{PEN}-\text{tan}}$ values between 1.20% and 25.38%.

Table 8 shows that during the rest phase, after the motion has ended, the number of sloshing masses has a negligible effect, and the difference between the PEN-rad and PEN-vert formulations becomes minimal. Overall, all formulations can both underestimate and overestimate the sloshing height, though PEN-rad and PEN-vert typically exhibit larger errors ($|\lambda_{\text{PEN}-\text{rad}}| > |\lambda_{\text{PEN}-\text{tan}}|$ and $|\lambda_{\text{PEN}-\text{vert}}| > |\lambda_{\text{PEN}-\text{tan}}|$ in most cases).

Based on these data, the tangent-based formulation emerges as the preferred method, as it consistently overestimates the sloshing height peak during motion ($\epsilon_{\text{PEN}-\text{tan}} > 0$ in all cases), and provides acceptable results during the rest phase. Fig. 14 clarifies the behavior of the different PEN formulations. These plots, which depict sloshing heights normalized by the container radius against varying pendulum angles $(\phi_{x1}, \phi_{y1}) \in [-30°, 30°] \times [-30°, 30°]$, distinctly show the overestimation characteristic of the PEN-tan formulation (in red) over the PEN-rad and PEN-vert ones (in blue and green, respectively).

Table 5 Values of ϵ from the PMD-model formulation ($\alpha = 0$) in the case $h/R = 1.6$

ϵ[%]	N	Se	Sc	Sg	Te	Tc	Tg
PMD	1	16.01	-15.39	0.59	-11.58	-0.45	5.28
	2	22.11	-8.99	8.05	-4.28	6.52	13.86
	3	24.55	-6.65	10.73	-1.50	9.20	16.97

Table 6 Values of λ from the PMD-model formulation ($\alpha = 0$) in the case $h/R = 1.6$

λ[%]	N	Se	Sc	Sg	Te	Tc	Tg
PMD	1	45.80	5.39	16.18	-0.71	10.51	41.96
	2	47.92	6.00	17.80	-0.70	10.88	44.67
	3	48.05	6.06	17.95	-0.70	10.92	45.20

Table 7 Values of ϵ from the PEN-model formulations in the case $h/R = 1.6$.

ϵ[%]	N	Se	Sc	Sg	Te	Tc	Tg
PEN-rad	1	-14.61	-32.40	-12.91	-27.35	-38.07	-37.76
	2	-9.21	-27.04	-6.10	-21.24	-33.06	-32.29
	3	-7.18	-25.02	3.62	-18.92	-31.15	-30.19
PEN-vert	1	-8.84	-28.52	-10.21	-23.88	-32.58	-32.38
	2	-3.28	-22.92	-3.24	-17.50	-27.21	-26.42
	3	-1.19	-20.82	-0.70	-15.07	-25.16	-24.13
PEN-tan	1	25.38	1.20	16.71	4.70	3.44	4.07

Table 8 Values of λ from the PEN-model formulations in the case $h/R = 1.6$.

λ[%]	N	Se	Sc	Sg	Te	Tc	Tg
PEN-rad	1	33.37	-13.92	-5.53	0.78	-1.92	-15.38
	2	34.75	-13.89	-4.68	0.85	-1.88	-15.16
	3	34.88	-13.89	-4.59	0.86	-1.88	-15.10
PEN-vert	1	33.67	-13.91	-5.51	0.78	-1.91	-15.30
	2	35.05	-13.89	-4.66	0.85	-1.88	-15.08
	3	35.17	-13.88	-4.57	0.86	-1.88	-15.02
PEN-tan	1	47.51	-9.34	2.08	2.68	0.83	-9.13

7.4 Comparison of the PMD and PEN models

Figure 15 compares the PMSD and PEN models in the case $h/R = 1.6$, using their respective optimal formulations, which ensure an overestimation of the sloshing height while providing reasonably accurate results. Specifically, the PMSD model uses three sloshing masses and no spring (PMD model), while the PEN model employs the PEN-tan sloshing-height formulation. In each subfigure, the blue line represents the experimental sloshing height extracted from the video-processing algorithm, whereas the green

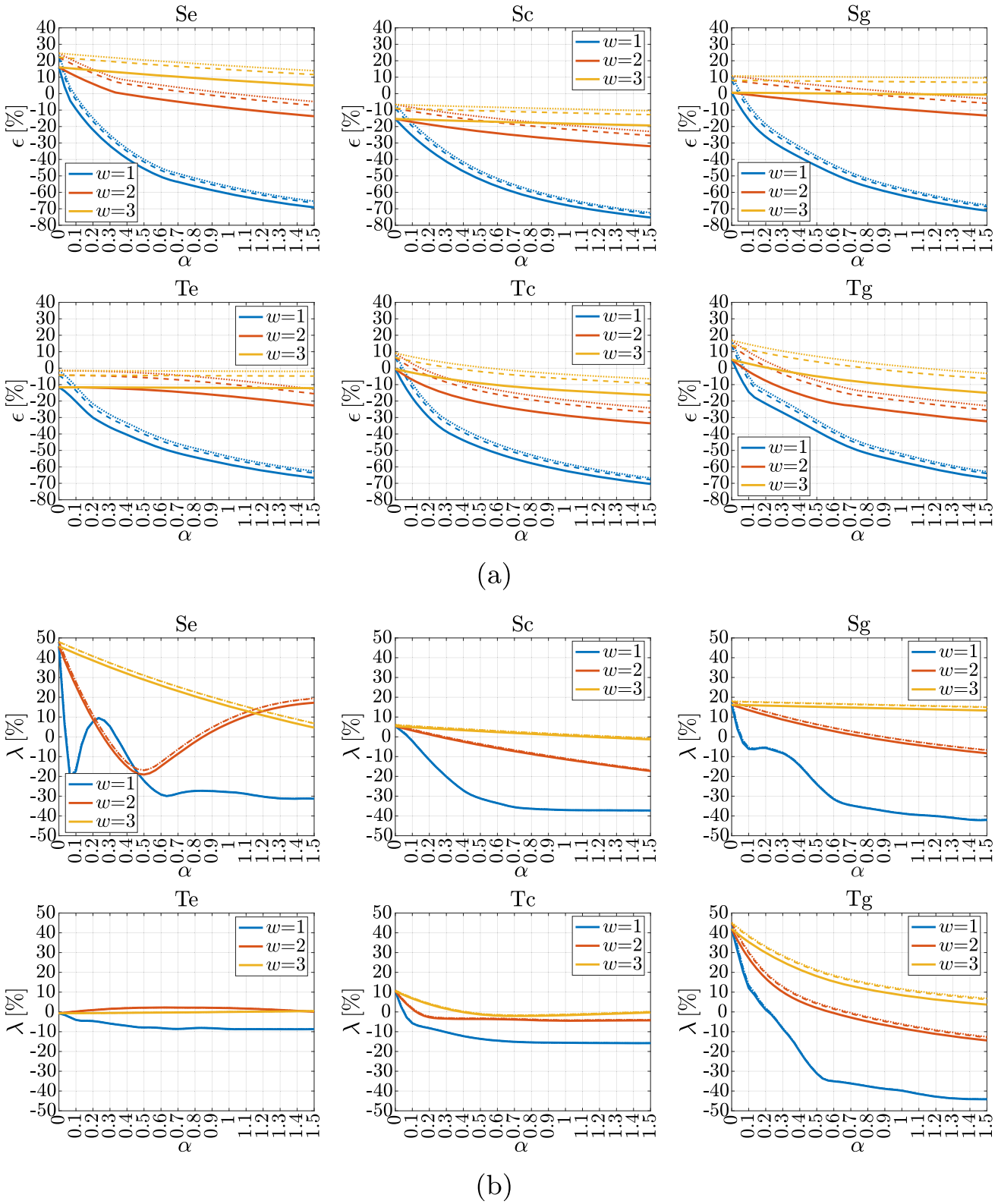

Fig. 13 Analysis of the accuracy-index trends for the PMSD model in the case $h/R = 1.6$: trends of ϵ (**a**) and λ (**b**) in terms of (α, w): the solid line corresponds to $N = 1$, the dashed line to $N = 2$, the dotted line to $N = 3$

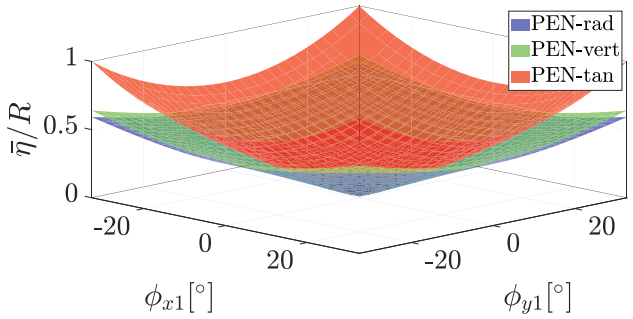

Fig. 14 Comparison of sloshing height predictions for PEN formulations

Table 9 Comparison for ϵ between the PMD and the PEN-tan formulations in the case $h/R = 1.6$.

ϵ[%]	N	Se	Sc	Sg	Te	Tc	Tg
PMD	3	24.55	-6.65	10.73	-1.50	9.20	16.97
PEN-tan	1	25.38	1.20	16.71	4.70	3.44	4.07

and purple lines illustrate the PMD and PEN-tan predictions, respectively. Both models exhibit a good adherence with the real-liquid behavior, especially during motion and near the sloshing-height maxima. During the rest phase, the PMD model overestimates the liquid-free oscillations in most cases, whereas the PEN-tan shows a less conservative prediction. These considerations find confirmation in Tables 9 and 10, which provide the comparison between the two models in terms of ϵ and λ, respectively.

The comparison of the PMD and PEN-tan predictions against the experimental sloshing height for the cases $h/R = 0.6$ and $h/R = 1$ are reported in Appendix A.2.3.

Table 10 Comparison for λ between the PMD and the PEN-tan formulations in the case $h/R = 1.6$.

λ[%]	N	Se	Sc	Sg	Te	Tc	Tg
PMD	3	48.05	6.06	17.95	-0.70	10.92	45.20
PEN-tan	1	47.51	-9.34	2.08	2.68	0.83	-9.13

Based on these results, we can infer that the PMD model with three sloshing masses and the PEN model using the tangent-based sloshing height formulation are fairly equivalent, with the former generally providing more conservative predictions. It is worth noting that the sloshing-height overestimation exhibited by the PMD model during the rest phase tends to increase as the h/R ratio decreases, whereas the PEN–tan formulation yields, in this phase, slightly more accurate, albeit less conservative, predictions.

8 Conclusions and future work

This paper extended previously developed models to predict the liquid sloshing height in a cylindrical container under two complex motion types: SCARA motion (3D translation combined with vertical-axis rotation) and tilting motion (3D translation with fixed-axis tilting rotation). The equivalent discrete sloshing models, namely the Paraboloidal Mass-Spring-Damper (PMSD) model and the Pendulum (PEN) model, inherited from our prior works [18, 25, 32], maintained their simplicity and computational efficiency, offering reliable and easy-to-compute sloshing-height estimations, even under complex and highly dynamical motions of the

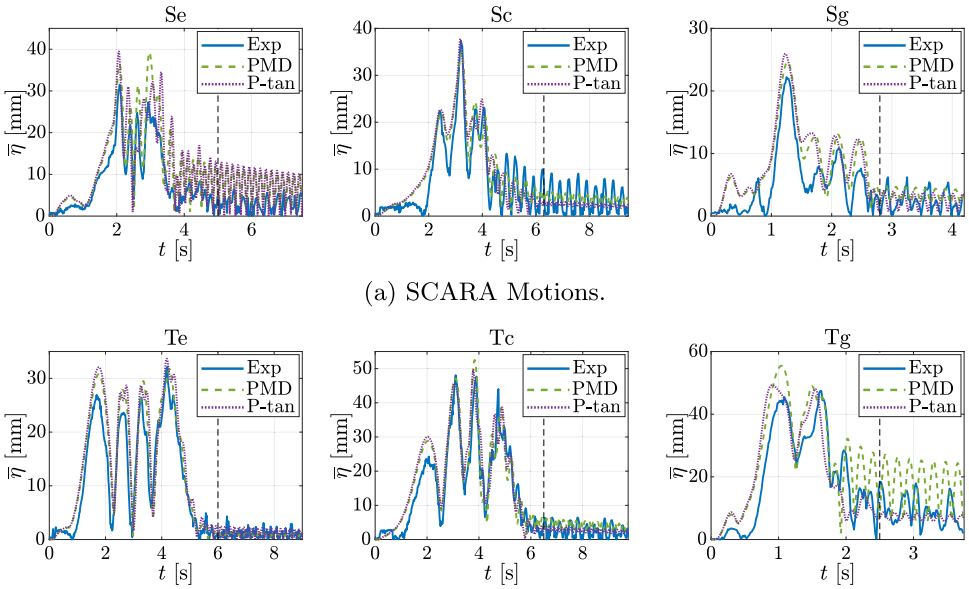

(a) SCARA Motions.

(b) Tilting Motions.

Fig. 15 Comparison of the PMD and PEN-tan predictions against the experimental sloshing height in the case $h/R = 1.6$

container, with accelerations up to 7.2m/s^2 and 11.0rad/s^2. We comprehensively examined and compared the agreement between the different variants of the two discrete models and the continuum model, highlighting their similarities, differences, and underlying physical relationships.

Experiments were conducted using an industrial robot executing several highly dynamic trajectories with different motion profiles, maintaining the liquid dynamics in a weakly nonlinear regime. The ratio of the static liquid height to the container radius was varied between 0.6 and 1.6. Two accuracy indices were defined to quantify the error between the model predictions and the experimental sloshing heights. Based on the experimental data, the best model variants were identified by evaluating the effect of model parameters and sloshing-height formulations on the prediction accuracy. For industrial applications (in which overestimating the liquid behavior is usually the most advisable option), the PMD model—obtained from the PMSD model by removing the spring—with three sloshing masses consistently provided the most reliable and conservative sloshing-height predictions. Among the proposed formulations for the PEN model, the tangent-based one proved to be the most effective choice as it conservatively overestimates the sloshing height.

The comparison between the PMD and the PEN-tan model revealed three key insights:

- the PMD model offered a robust evaluation of the sloshing height across all motion types, reliably predicting trends while providing a conservative estimation of sloshing peaks, even during the rest phase;
- the PMD model is more accurate during the motion phase than during the rest phase, with the sloshing-height overestimation during rest becoming more pronounced as the h/R ratio decreases;
- the tangent-based PEN model generally performs as well as the PMD model, consistently overestimating the sloshing height. However, during the rest phase, it tends to produce less conservative estimates. An advantage of this model is its simplicity, which makes it both intuitive and independent of any model parameter.

The results of this paper may be especially useful to build efficient optimization algorithms for anti-sloshing trajectory planning.

Future work will focus on extending this approach to $6D$ motions of cylindrical containers. Additional investigations will address sloshing models for parallelepiped-like containers subjected to SCARA and tilting motions.

Appendix A

A.1 CoM coordinates in the continuum model

To compute the CoM coordinates for the case at hand and to consider all sloshing modes, the authors drew inspiration from the literature [14, 26], where only 1D excitation and the first sloshing mode were considered. The CoM coordinates in the continuum model, provided in Eq. (11), can be obtained by solving the integrals in Eq. (10), where the following properties of the Bessel functions can be exploited [38]:

$$\int_0^R r^2 \frac{J_1(\xi_n \frac{r}{R})}{J_1(\xi_n)}\, dr = \frac{R^3}{\xi_n^2}, \tag{A.1a}$$

$$\int_0^R r \frac{J_1^2\left(\xi_n \frac{r}{R}\right)}{J_1^2\left(\xi_n\right)} dr = \frac{R^2\left(\xi_n^2 - 1\right)}{2\xi_{1n}^2}, \tag{A.1b}$$

$$\int_0^R r \frac{J_1\left(\xi_n \frac{r}{R}\right)}{J_1\left(\xi_n\right)} \frac{J_1\left(\xi_{1k} \frac{r}{R}\right)}{J_1\left(\xi_{1k}\right)} dr = 0, n \neq k. \tag{A.1c}$$

In particular, substituting the free-surface description in Eq. (8) into the CoM coordinates x_G and y_G expressed in Eq. (10a) and (10b) yields:

$$\begin{aligned}
x_G &= \frac{1}{\pi R^2 h} \int_0^{2\pi} \int_0^R \int_{-\frac{h}{2}}^{\frac{h}{2}+\eta} r^2 \cos\phi dz dr d\phi = \\
&= \frac{1}{\pi R^2 h} \int_0^{2\pi} \int_0^R (h+\eta) r^2 \cos\phi dr d\phi = \\
&= \frac{1}{\pi R^2 h} \int_0^{2\pi} \int_0^R \left[h r^2 \cos\phi + \sum_{n=1}^{\infty} \overline{\eta}_n r^2 \frac{J_1\left(\xi_n \frac{r}{R}\right)}{J_1\left(\xi_n\right)} \cos\phi \cos\left(\phi - \phi_n\right) \right] dr d\phi = \\
&= \frac{1}{\pi R^2 h} \int_0^{2\pi} \left[\sum_{n=1}^{\infty} \overline{\eta}_n \frac{R^3}{\xi_n^2} \left(\cos^2\phi \cos\phi_n + \cos\phi \sin\phi \sin\phi_n \right) \right] d\phi = \\
&= \frac{1}{\pi R^2 h} \pi R^3 \sum_{n=1}^{\infty} \frac{\overline{\eta}_n}{\xi_n^2} \cos\phi_n = \frac{R}{h} \sum_{n=1}^{\infty} \frac{\overline{\eta}_n}{\xi_n^2} \cos\phi_n,
\end{aligned} \tag{A.2}$$

$$\begin{aligned}
y_G &= \frac{1}{\pi R^2 h} \int_0^{2\pi} \int_0^R \int_{-\frac{h}{2}}^{\frac{h}{2}+\eta} r^2 \sin\phi dz dr d\phi = \\
&= \frac{1}{\pi R^2 h} \int_0^{2\pi} \int_0^R (h+\eta) r^2 \sin\phi dr d\phi = \\
&= \frac{1}{\pi R^2 h} \int_0^{2\pi} \int_0^R \left[h r^2 \sin\phi + \sum_{n=1}^{\infty} \overline{\eta}_n r^2 \frac{J_1\left(\xi_n \frac{r}{R}\right)}{J_1\left(\xi_n\right)} \times \right. \\
&\left. \times \sin\phi \cos\left(\phi - \phi_n\right) \right] dr d\phi = \\
&= \frac{1}{\pi R^2 h} \int_0^{2\pi} \left[\sum_{n=1}^{\infty} \overline{\eta}_n \frac{R^3}{\xi_n^2} \left(\sin\phi \cos\phi \cos\phi_n + \sin^2\phi \sin\phi_n \right) \right] d\phi = \\
&= \frac{1}{\pi R^2 h} \pi R^3 \sum_{n=1}^{\infty} \frac{\overline{\eta}_n}{\xi_n^2} \sin\phi_n = \frac{R}{h} \sum_{n=1}^{\infty} \frac{\overline{\eta}_n}{\xi_n^2} \sin\phi_n,
\end{aligned} \tag{A.3}$$

where the following intermediate results have been omitted for the sake of brevity, namely:

$$\int_0^{2\pi}\int_0^R hr^2\cos\phi dr d\phi = \left[h\frac{R^3}{3}\sin\phi\right]_0^{2\pi} = 0, \quad \text{(A.4a)}$$

$$\int_0^{2\pi}\int_0^R hr^2\sin\phi dr d\phi = \left[-h\frac{R^3}{3}\cos\phi\right]_0^{2\pi} = 0, \quad \text{(A.4b)}$$

$$\int_0^{2\pi}\sum_{n=1}^{\infty}\overline{\eta}_n\frac{R^3}{\xi_n^2}\cos\phi\sin\phi\sin\phi_n d\phi =$$
$$= -\sum_{n=1}^{\infty}\overline{\eta}_n\frac{R^3}{\xi_n^2}\sin\phi_n\left[\frac{\cos 2\phi}{4}\right]_0^{2\pi} = 0, \quad \text{(A.4c)}$$

$$\int_0^{2\pi}\sum_{n=1}^{\infty}\overline{\eta}_n\frac{R^3}{\xi_n^2}\sin\phi\cos\phi\cos\phi_n d\phi =$$
$$= -\sum_{n=1}^{\infty}\overline{\eta}_n\frac{R^3}{\xi_n^2}\cos\phi_n\left[\frac{\cos 2\phi}{4}\right]_0^{2\pi} = 0, \quad \text{(A.4d)}$$

$$\int_0^{2\pi}\sum_{n=1}^{\infty}\overline{\eta}_n\frac{R^3}{\xi_n^2}\cos^2\phi\cos\phi_n d\phi =$$
$$= \sum_{n=1}^{\infty}\overline{\eta}_n\frac{R^3}{\xi_n^2}\cos\phi_n\left[\frac{1}{2}\phi+\frac{\sin 2\phi}{4}\right]_0^{2\pi} =$$
$$= \pi\sum_{n=1}^{\infty}\overline{\eta}_n\frac{R^3}{\xi_n^2}\cos\phi_n, \quad \text{(A.4e)}$$

$$\int_0^{2\pi}\sum_{n=1}^{\infty}\overline{\eta}_n\frac{R^3}{\xi_n^2}\sin^2\phi\sin\phi_n d\phi =$$
$$= \sum_{n=1}^{\infty}\overline{\eta}_n\frac{R^3}{\xi_n^2}\cos\phi_n\left[\frac{1}{2}\phi-\frac{\sin 2\phi}{4}\right]_0^{2\pi} =$$
$$= \pi\sum_{n=1}^{\infty}\overline{\eta}_n\frac{R^3}{\xi_n^2}\sin\phi_n. \quad \text{(A.4f)}$$

Similarly, substituting the free-surface description in Eq. (8) into the formulation of z_G in Eq. (10c) provides:

$$z_G = \frac{1}{\pi R^2 h}\int_0^{2\pi}\int_0^R\int_{-\frac{h}{2}}^{\frac{h}{2}+\eta(r,\phi,\overline{\eta}_n)} zr\,dz dr d\phi =$$
$$= \frac{1}{\pi R^2 h}\int_0^{2\pi}\int_0^R\frac{1}{2}\left(\eta h+\eta^2\right)r\,dr d\phi =$$
$$= \frac{1}{2\pi R^2 h}\int_0^{2\pi}\int_0^R h\left(\sum_{n=1}^{\infty}\overline{\eta}_n\frac{J_1\left(\xi_n\frac{r}{R}\right)}{J_1(\xi_n)}\cos(\phi-\phi_n)\right)r dr d\phi +$$
$$+\frac{1}{2\pi R^2 h}\int_0^{2\pi}\int_0^R\left(\sum_{n=1}^{\infty}\overline{\eta}_n\frac{J_1\left(\xi_n\frac{r}{R}\right)}{J_1(\xi_n)}\cos(\phi-\phi_n)\right)^2 r dr d\phi =$$
$$= \frac{1}{2\pi R^2 h}\int_0^{2\pi}\int_0^R\left(\sum_{n=1}^{\infty}r\overline{\eta}_n^2\frac{J_1^2\left(\xi_n\frac{r}{R}\right)}{J_1^2(\xi_n)}\cos^2(\phi-\phi_n)\right)dr d\phi +$$
$$+\frac{1}{2\pi R^2 h}\int_0^{2\pi}\int_0^R 2r\sum_{k=2}^{\infty}\sum_{n=1}^{k-1}\overline{\eta}_n\overline{\eta}_k\frac{J_1\left(\xi_n\frac{r}{R}\right)}{J_1(\xi_n)}\frac{J_1\left(\xi_{1k}\frac{r}{R}\right)}{J_1(\xi_{1k})}\times$$
$$\times\cos(\phi-\phi_n)\cos(\phi-\phi_k)dr d\phi =$$
$$= \frac{1}{2\pi R^2 h}\int_0^{2\pi}\sum_{n=1}^{\infty}\overline{\eta}_n^2\frac{R^2\left(\xi_n^2-1\right)}{2\xi_n^2}\left(\cos^2\phi\cos^2\phi_n+\sin^2\phi\sin^2\phi_n\right)d\phi +$$
$$+\frac{1}{2\pi R^2 h}\int_0^{2\pi}\sum_{n=1}^{\infty}\overline{\eta}_n^2\frac{R^2\left(\xi_n^2-1\right)}{2\xi_n^2}\left(2\cos\phi\sin\phi\cos\phi_n\sin\phi_n\right)d\phi =$$
$$= \frac{1}{2\pi R^2 h}\sum_{n=1}^{\infty}\overline{\eta}_n^2\frac{R^2\left(\xi_n^2-1\right)}{2\xi_n^2}\left\{\left[\frac{1}{2}\phi+\frac{\sin 2\phi}{4}\right]_0^{2\pi}\cos^2\phi_n +\right.$$
$$\left.+\left[\frac{1}{2}\phi-\frac{\sin 2\phi}{4}\right]_0^{2\pi}\sin^2\phi_n\right\} =$$
$$= \frac{1}{4\pi R^2 h}\pi R^2\sum_{n=1}^{\infty}\overline{\eta}_n^2\frac{\left(\xi_n^2-1\right)}{\xi_n^2} = \frac{1}{4h}\sum_{n=1}^{\infty}\overline{\eta}_n^2\frac{\left(\xi_n^2-1\right)}{\xi_n^2}, \quad \text{(A.5)}$$

where the following intermediate results have been omitted in Eq. (A.5):

$$\int_0^{2\pi}\int_0^R\sum_{n=1}^{\infty}\overline{\eta}_n\frac{J_1\left(\xi_n\frac{r}{R}\right)}{J_1(\xi_n)}\cos(\phi-\phi_n)r dr d\phi =$$
$$= \int_0^R\int_0^{2\pi}\sum_{n=1}^{\infty}\overline{\eta}_n r\frac{J_1\left(\xi_n\frac{r}{R}\right)}{J_1(\xi_n)}(\cos\phi\cos\phi_n+\sin\phi\sin\phi_n)d\phi dr =$$
$$= \int_0^R\sum_{n=1}^{\infty}\overline{\eta}_n r\frac{J_1\left(\xi_n\frac{r}{R}\right)}{J_1(\xi_n)}\left\{[\sin\phi]_0^{2\pi}\cos\phi_n-[\cos\phi]_0^{2\pi}\sin\phi_n\right\}dr = 0 \quad \text{(A.6a)}$$

$$\int_0^{2\pi}\sum_{n=1}^{\infty}\overline{\eta}_n^2\frac{R^2\left(\xi_n^2-1\right)}{2\xi_n^2}\left(2\cos\phi\sin\phi\cos\phi_n\sin\phi_n\right)d\phi =$$
$$= -\sum_{n=1}^{\infty}\overline{\eta}_n^2\frac{R^2\left(\xi_n^2-1\right)}{2\xi_n^2}\cos\phi_n\sin\phi_n\left[\frac{\cos 2\phi}{2}\right]_0^{2\pi} = 0. \quad \text{(A.6b)}$$

A.2 Experimental results for $h/R = 0.6$ and $h/R = 1$

This appendix reports the experimental results for the cases $h/R = 0.6$ and $h/R = 1$.

A.2.1 PMSD model

The accuracy indices ϵ and λ for the PMSD model are analyzed for $\alpha \in [0, 1.5]$, $w \in \{1, 2, 3\}$, and $N \in \{1, 2, 3\}$. Figures 16a and 16b show $\epsilon(\alpha, w)$ and $\lambda(\alpha, w)$ for the Se, Sc, Sg, Te, Tc, and Tg motions in the case $h/R = 0.6$, whereas Figs. 17a and 17b report the corresponding results for $h/R = 1$. In each plot, blue, red, and yellow curves correspond to $w = 1$, $w = 2$, and $w = 3$, respectively; for each color, solid, dashed, and dotted lines denote $N = 1$, $N = 2$, and $N = 3$.

A.2.2 PEN model

Results for the accuracy indices ϵ and λ of the PEN model are summarized in Tables 11 and 12 for the case $h/R = 0.6$, and in Tables 13 and 14 for the case $h/R = 1$.

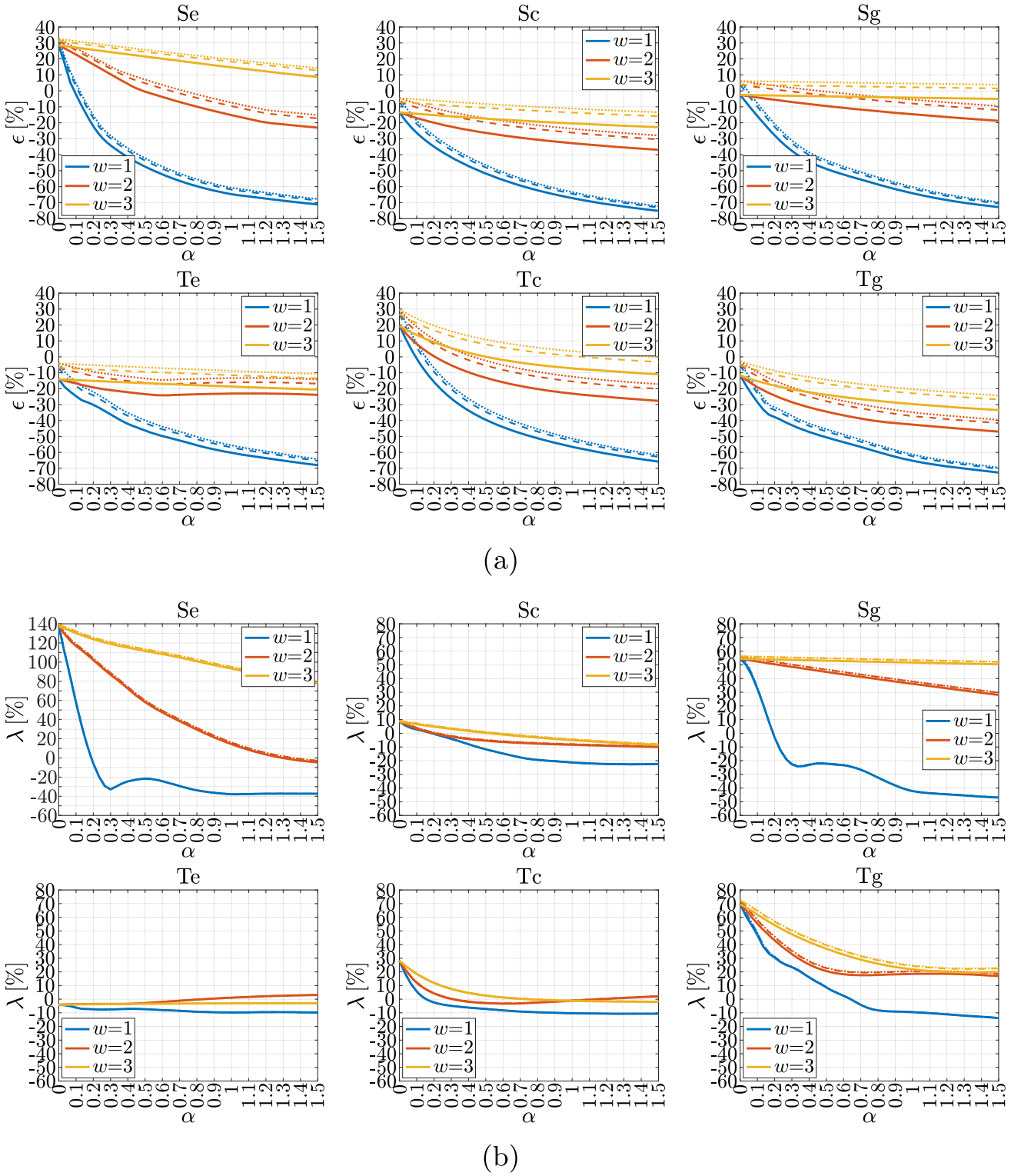

Fig. 16 Accuracy-index trends for the PMSD model in the case $h/R = 0.6$: ϵ (**a**) and λ (**b**) as functions of (α, w). For each w, solid, dashed, and dotted lines correspond to $N = 1$, $N = 2$, and $N = 3$, respectively

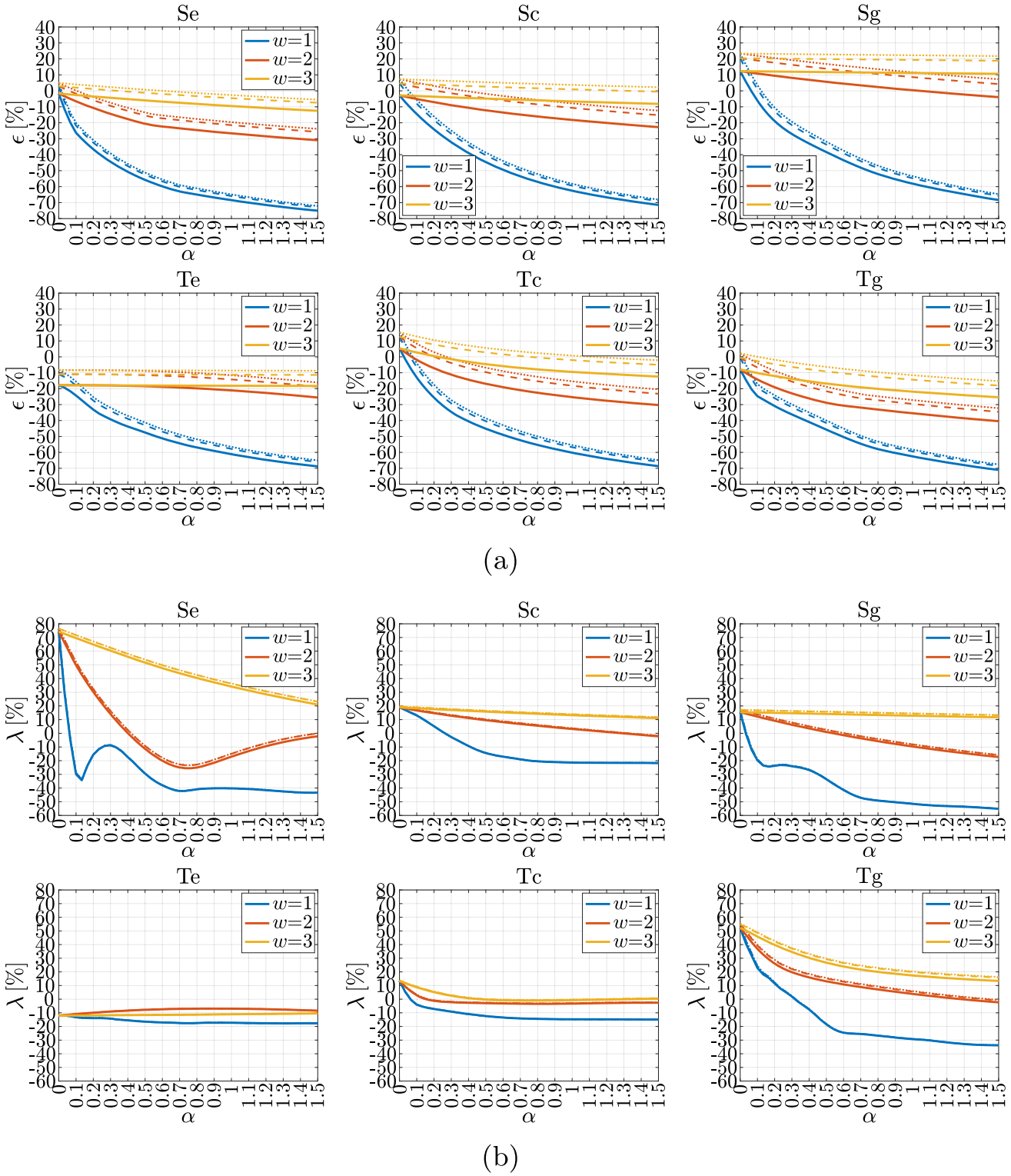

Fig. 17 Accuracy-index trends for the PMSD model in the case $h/R = 1$: ϵ (**a**) and λ (**b**) as functions of (α, w). For each w, solid, dashed, and dotted lines correspond to $N = 1$, $N = 2$, and $N = 3$, respectively

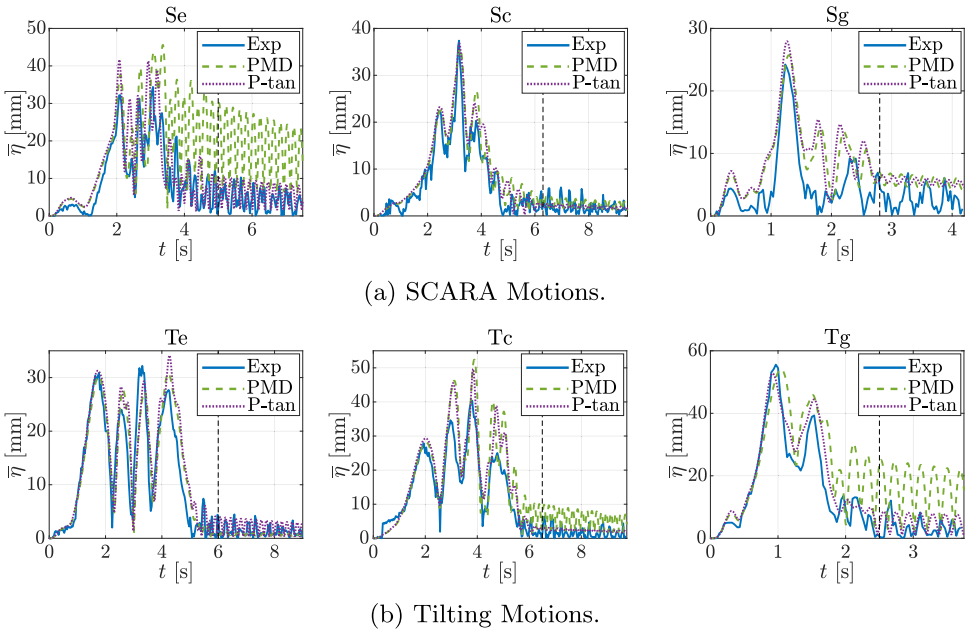

(a) SCARA Motions.

(b) Tilting Motions.

Fig. 18 Comparison of the PMD and PEN-tan predictions against the experimental sloshing height in the case $h/R = 0.6$

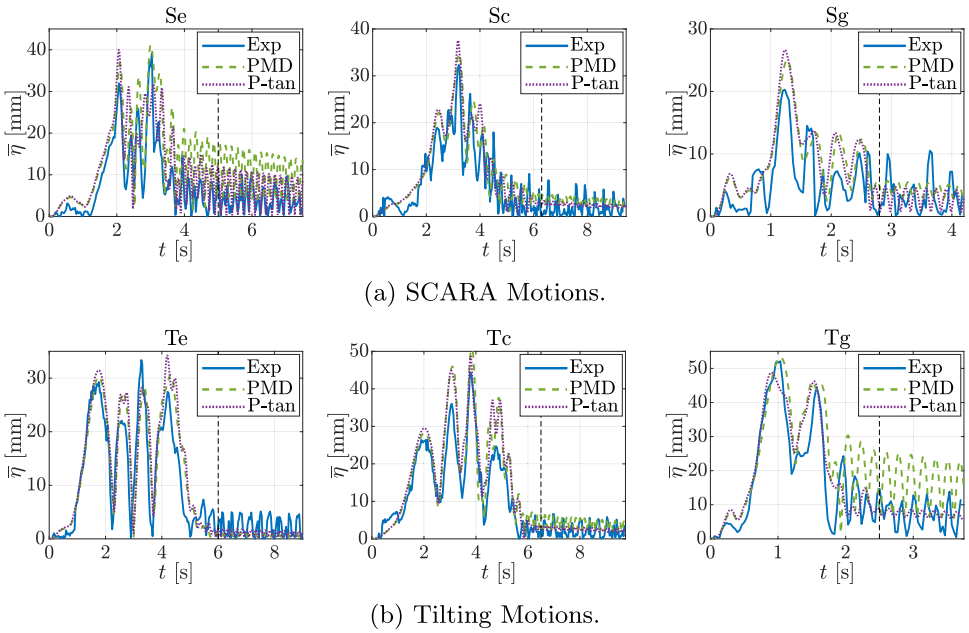

(a) SCARA Motions.

(b) Tilting Motions.

Fig. 19 Comparison of the PMD and PEN-tan predictions against the experimental sloshing height in the case $h/R = 1$

Table 11 Values of ϵ from the PEN-model formulations in the case $h/R = 0.6$

ϵ[%]	N	Se	Sc	Sg	Te	Tc	Tg
PEN-rad	1	-19.14	-33.63	-14.55	-25.84	-26.42	-44.95
	2	-14.45	-28.32	-8.53	-19.87	-20.59	-40.42
	3	-12.58	-26.31	-6.32	-17.58	-18.36	-38.70
PEN-vert	1	-13.17	-29.96	-11.46	-22.11	-19.94	-39.67
	2	-8.35	-24.41	-5.31	-15.89	-13.70	-34.78
	3	-6.43	-22.32	-3.06	-13.50	-11.32	-32.92
PEN-tan	1	21.08	-1.59	15.23	6.10	23.09	-4.99

Table 12 Values of λ from the PEN-model formulations in the case $h/R = 0.6$

λ[%]	N	Se	Sc	Sg	Te	Tc	Tg
PEN-rad	1	8.94	-2.98	38.42	4.40	2.56	7.41
	2	10.09	-2.96	39.33	4.45	2.58	7.70
	3	10.19	-2.95	39.42	4.46	2.58	7.75
PEN-vert	1	9.08	-2.98	38.56	4.40	2.56	7.47
	2	10.23	-2.95	39.47	4.46	2.58	7.76
	3	10.34	-2.95	39.57	4.47	2.58	7.81
PEN-tan	1	18.80	0.87	56.33	7.21	5.18	12.41

Table 13 Values of ϵ from the PEN-model formulations in the case $h/R = 1$

ϵ[%]	N	Se	Sc	Sg	Te	Tc	Tg
PEN-rad	1	-30.79	-22.17	-2.53	-28.93	-33.62	-43.84
	2	-26.51	-16.01	4.91	-23.11	-28.26	-38.99
	3	-24.87	-13.69	7.62	-20.89	-26.21	-37.14
PEN-vert	1	-26.02	-17.73	0.64	-25.41	-27.90	-39.09
	2	-21.61	-11.30	8.26	-19.34	-22.16	-33.84
	3	-19.92	-8.87	11.03	-17.03	-19.97	-31.84
PEN-tan	1	2.07	16.17	31.30	2.69	9.76	-6.39

Table 14 Values of λ from the PEN-model formulations in the case $h/R = 1$

λ[%]	N	Se	Sc	Sg	Te	Tc	Tg
PEN-rad	1	16.85	3.35	-14.40	-10.40	-0.07	-3.06
	2	18.24	3.38	-13.57	-10.34	-0.05	-2.80
	3	18.36	3.38	-13.49	-10.33	-0.05	-2.75
PEN-vert	1	17.08	3.36	-14.37	-10.40	-0.07	-2.96
	2	18.47	3.38	-13.54	-10.34	-0.05	-2.71
	3	18.60	3.39	-13.46	-10.33	-0.04	-2.65
PEN-tan	1	29.73	8.28	-5.92	-8.95	2.86	3.59

Table 15 Comparison for ϵ between the PMD and the PEN-tan formulations in the case $h/R = 0.6$.

ϵ[%]	N	Se	Sc	Sg	Te	Tc	Tg
PMD	3	32.55	-4.45	6.17	-4.16	29.74	-2.69
PEN-tan	1	21.08	-1.59	15.23	6.10	23.09	-4.99

Table 16 Comparison for λ between the PMD and the PEN-tan formulations in the case $h/R = 0.6$.

λ[%]	N	Se	Sc	Sg	Te	Tc	Tg
PMD	3	139.18	9.30	56.34	-4.04	28.38	72.61
PEN-tan	1	18.80	0.87	56.33	7.21	5.18	12.41

A.2.3 Comparison of the PMD and PEN models

Figure 18 compares the PMD and PEN models in the case $h/R = 0.6$, using their respective optimal formulations. Specifically, the PMD model uses three sloshing masses (and no spring), while the PEN model employs the PEN-tan sloshing-height formulation. In each subfigure, the blue line represents the experimental sloshing height extracted using the video-processing algorithm, whereas the green and purple lines show the PMD and PEN-tan predictions, respectively. Tables 15 and 16 provide the comparison between the two models in terms of ϵ and λ, respectively.

Table 17 Comparison for ϵ between the PMD and the PEN-tan formulations in the case $h/R = 1$

ϵ[%]	N	Se	Sc	Sg	Te	Tc	Tg
PMD	3	4.95	7.33	23.34	-8.29	15.46	2.23
PEN-tan	1	2.07	16.17	31.30	2.69	9.76	-6.39

Table 18 Comparison for λ between the PMD and the PEN-tan formulations in the case $h/R = 1$

λ[%]	N	Se	Sc	Sg	Te	Tc	Tg
PMD	3	76.56	19.67	17.17	-11.99	13.79	55.31
PEN-tan	1	29.73	8.28	-5.92	-8.95	2.86	3.59

Figure 19, Table 17 and 18 compare the PMD and PEN models in the case $h/R = 1$.

Author Contributions Conceptualization: R.D.L., S.S., L.B., M.C.; investigation: R.D.L., S.S.; methodology: R.D.L., S.S., L.B., M.C.; software: R.D.L., S.S.; writing - original draft: R.D.L., S.S.; writing - review & editing: M.C., L.B.; supervision: M.C., L.B.; project administration: M.C., G.P.; resources: M.C., G.P.

Funding Open access funding provided by Alma Mater Studiorum - Università di Bologna within the CRUI-CARE Agreement. This study was carried out within the FISA 2023-00210 project "APACHE – Advanced manipulation, grasping and control for enhanced machinery autonomy and reconfigurability in pharmaceutical processes and e-commerce packaging" (FISA Call dated 01/08/2023, No. 1233 – Decree No. 6949 of 15/04/2025 – CUP J53C25000520001) funded by the Italian Ministry of University and Research (MUR).
This work was also partially supported by the PRIN 2020 project "Co-Mir – Extending Robotic Manipulation Capabilities by Cooperative Mobile and Flexible Multi-Robot Systems" (project code: 2020CMEFPK).

Data Availability The datasets generated and analysed during the current study are available in the "Sloshing-Height Estimation for Liquid-filled Containers under Four-Dimensional Motions Including Spatial Translation and Rotation about a Fixed Direction: Modelling and Experimental Validation" repository, https://doi.org/10.5281/zenodo.16578372

Declarations

Competing interests The authors declare no competing interests.

References

1. Aribowo, W., Yamashita, T., Terashima, K.: Integrated trajectory planning and sloshing suppression for three-dimensional motion of liquid container transfer robot arm. Journal of Robotics 2015, 279460–279474 (2015) https://doi.org/10.1155/2015/279460
2. Terashima, K., Yano, K.: Sloshing analysis and suppression control of tilting-type automatic pouring machine. Control. Eng. Pract. **9**(6), 607–620 (2001). https://doi.org/10.1016/S0967-0661(01)00023-5
3. Kaneko, M., Sugimoto, Y., Yano, K., Terashima, K.: Supervisory control of pouring process by tilting-type automatic pouring robot. In: Proceedings of the 2003 IEEE/RSJ International Conference on Intelligent Robots and Systems (IROS), Las Vegas, NV, USA, pp. 3004–3009 (2003). https://doi.org/10.1109/IROS.2003.1249328
4. Kolukula, S.S., Chellapandi, P.: Nonlinear finite element analysis of sloshing. Adv. Numer. Anal. **2013**, 1–10 (2013). https://doi.org/10.1155/2013/571528
5. Wang, C.Z., Khoo, B.C.: Finite element analysis of two-dimensional nonlinear sloshing problems in random excitations. Ocean Eng. **32**(2), 107–133 (2005). https://doi.org/10.1016/j.oceaneng.2004.08.001
6. Schörgenhumer, M., Eitzlmayr, A.: Modeling of liquid sloshing with application in robotics and automation. IFAC-PapersOnLine **52**(15), 253–258 (2019). https://doi.org/10.1016/j.ifacol.2019.11.683
7. Green, M.D., Peiró, J.: Long duration sph simulations of sloshing in tanks with a low fill ratio and high stretching. Computers & Fluids **174**, 179–199 (2018). https://doi.org/10.1016/j.compfluid.2018.07.006
8. Liu, D., Lin, P.: A numerical study of three-dimensional liquid sloshing in tanks. J. Comput. Phys. **227**(8), 3921–3939 (2008). https://doi.org/10.1016/j.jcp.2007.12.006
9. Huang, J., Zhao, X.: Control of three-dimensional nonlinear slosh in moving rectangular containers. J. Dyn. Syst. Meas. Contr. **140**(8), 081016–081023 (2018). https://doi.org/10.1115/1.4039278
10. Faltinsen, O.M., Rognebakke, O.F., Timokha, A.N.: Resonant three-dimensional nonlinear sloshing in a square-base basin. J. Fluid Mech. **487**, 1–42 (2003). https://doi.org/10.1017/S0022112003004816
11. Ardakani, H.A., Bridges, T.J.: Shallow-water sloshing in vessels undergoing prescribed rigid-body motion in three dimensions. J. Fluid Mech. **667**, 474–519 (2011). https://doi.org/10.1017/S0022112010004477
12. Moya, B., Gonzalez, D., Alfaro, I., Chinesta, F., Cueto, E.: Learning slosh dynamics by means of data. Comput. Mech. **64**(2), 511–523 (2019). https://doi.org/10.1007/s00466-019-01705-3
13. Moya, B., Alfaro, I., Gonzalez, D., Chinesta, F., Cueto, E.: Physically sound, self-learning digital twins for sloshing fluids. PLoS ONE **15**(6), 1–16 (2020). https://doi.org/10.1371/journal.pone.0234569
14. Ibrahim, R.A.: Liquid sloshing dynamics: theory and applications. Cambridge University Press, New York, NY (2005). https://doi.org/10.1017/CBO9780511536656
15. Reinhold, J., Amersdorfer, M., Meurer, T.: A dynamic optimization approach for sloshing free transport of liquid filled containers using an industrial robot. In: Proceedings of the 2019 IEEE/RSJ International Conference on Intelligent Robots and Systems (IROS), Macau, China, pp. 2336–2341 (2019). https://doi.org/10.1109/IROS40897.2019.8968144
16. Moriello, L., Biagiotti, L., Melchiorri, C., Paoli, A.: Control of liquid handling robotic systems: A feed-forward approach to suppress sloshing. In: Proceedings of the 2017 IEEE International Conference on Robotics and Automation (ICRA), Singapore, pp. 4286–4291 (2017). https://doi.org/10.1109/ICRA.2017.7989493
17. Moriello, L., Biagiotti, L., Melchiorri, C., Paoli, A.: Manipulating liquids with robots: A sloshing-free solution. Control. Eng. Pract. **78**, 129–141 (2018). https://doi.org/10.1016/j.conengprac.2018.06.018
18. Biagiotti, L., Chiaravalli, D., Moriello, L., Melchiorri, C.: A plug-in feed-forward control for sloshing suppression in robotic teleoperation tasks. In: Proceedings of the 2018 IEEE/RSJ International Conference on Intelligent Robots and Systems (IROS), Madrid, Spain, pp. 5855–5860 (2018). https://doi.org/10.1109/IROS.2018.8593962
19. Hamaguchi, M., Taniguchi, T.: Transfer control and curved path design for cylindrical liquid container. IFAC Proceedings Volumes **35**(1), 79–84 (2002). https://doi.org/10.3182/20020721-6-es-1901.01481
20. Hamaguchi, M., Yoshida, Y., Kihara, T., Taniguchi, T.: Path design and trace control of a wheeled mobile robot to damp liquid sloshing in a cylindrical container. In: Proceedings of the 2005 IEEE International Conference Mechatronics and Automation, Niagara Falls, ON, Canada, pp. 1959–1964 (2005). https://doi.org/10.1109/icma.2005.1626862
21. Maderna, R., Casalino, A., Zanchettin, A.M., Rocco, P.: Robotic handling of liquids with spilling avoidance: A constraint-based control approach. In: Proceedings of the 2018 IEEE International Conference on Robotics and Automation (ICRA), Brisbane, QLD, Australia, pp. 7414–7420 (2018). https://doi.org/10.1109/icra.2018.8460927
22. Pridgen, B., Bai, K., Singhose, W.: Shaping container motion for multimode and robust slosh suppression. J. Spacecr. Rocket. **50**(2), 440–448 (2013). https://doi.org/10.2514/1.a32137
23. Hervas, J.R., Reyhanoglu, M.: Observer-based nonlinear control of space vehicles with multi-mass fuel slosh dynamic. In: Proceedings of the 2014 IEEE 23rd International Symposium on Industrial Electronics (ISIE), Istanbul, Turkey, pp. 178–182 (2014). https://doi.org/10.1109/ISIE.2014.6864607
24. Reyhanoglu, M., Rubio Hervas, J.: Nonlinear dynamics and control of space vehicles with multiple fuel slosh modes. Control. Eng. Pract. **20**(9), 912–918 (2012). https://doi.org/10.1016/j.conengprac.2012.05.011
25. Guagliumi, L., Berti, A., Monti, E., Carricato, M.: A simple model-based method for sloshing estimation in liquid transfer in automatic machines. IEEE Access 9, 129347–129357 (2021) https://doi.org/10.1109/ACCESS.2021.3113956
26. Bauer, H.: Nonlinear mechanical model for the description of propellant sloshing. AIAA J. **4**, 1662–1668 (1966)
27. Guagliumi, L., Berti, A., Monti, E., Carricato, M.: Anti-sloshing trajectories for high-acceleration motions in automatic machines. J. Dyn. Syst. Meas. Contr. **144**(7), 071006–071015 (2022). https://doi.org/10.1115/1.4054224
28. Brasina, F., Guagliumi, L., Di Leva, R., Carricato, M.: Anti-sloshing motion laws for one-dimensional piecewise trajectories. In: New Trends in Mechanism and Machine Science - Proceedings of EuCoMeS 2024. Mechanisms and Machine Science, vol. 165, pp. 153–162 (2024). https://doi.org/10.1007/978-3-031-67295-8_18
29. Guagliumi, L., Berti, A., Monti, E., Carricato, M.: A software application for fast liquid-sloshing simulation. In: Niola, V., Gasparetto, A., Quaglia, G., Carbone, G. (eds.) Advances in Italian Mechanism Science - Proceedings of the IFToMM Italy 2022. Mechanisms and Machine Science, vol. 122, pp. 819–828. Springer, Cham (2022). https://doi.org/10.1007/978-3-031-10776-4_94
30. Di Leva, R., Carricato, M., Gattringer, H., Müller, A.: Sloshing dynamics estimation for liquid-filled containers under 2-dimensional excitation. In: Proceedings of the 10th ECCOMAS Thematic Conference on MULTIBODY DYNAMICS,

Budapest, Hungary, pp. 80–89 (2021). https://doi.org/10.3311/eccomasmbd2021-274
31. Di Leva, R., Carricato, M., Gattringer, H., Muller, A.: Time-optimal trajectory planning for anti-sloshing 2-dimensional motions of an industrial robot. In: Proceedings of the 2021 20th International Conference on Advanced Robotics (ICAR), Ljubljana, Slovenia, pp. 32–37 (2021). https://doi.org/10.1109/icar53236.2021.9659383
32. Di Leva, R., Carricato, M., Gattringer, H., Müller, A.: Sloshing dynamics estimation for liquid-filled containers performing 3-dimensional motions: modeling and experimental validation. Multibody Sys.Dyn. **56**(2), 153–171 (2022). https://doi.org/10.1007/s11044-022-09841-0
33. Di Leva, R., Soprani, S., Palli, G., Biagiotti, L., Carricato, M.: Sloshing-height estimation for liquid-filled containers under four-dimensional motions including spatial translation and rotation about a fixed direction: Modelling and experimental validation. [Data set] Zenodo (2025) https://doi.org/10.5281/zenodo.16578372
34. Bauer, H.F.: Tables of zeros of cross product Bessel functions. Math. Comput. **18**(85), 128–135 (1964). https://doi.org/10.1090/S0025-5718-1964-0158105-5
35. Dodge, F.T.: The New "Dynamic behavior of liquids in moving containers". Southwest Research Institute, San Antonio, Texas (2000)
36. Muchacho, R.I.C., Laha, R., Figueredo, L.F.C., Haddadin, S.: A solution to slosh-free robot trajectory optimization. In: 2022 IEEE/RSJ International Conference on Intelligent Robots and Systems (IROS), Kyoto, Japan, pp. 223–230 (2022). https://doi.org/10.1109/iros47612.2022.9981173
37. Yano, K., Higashikawa, S., Terashima, K.: Liquid container transfer control on 3D transfer path by hybrid shaped approach. In: Proceedings of the 2001 IEEE International Conference on Control Applications (CCA), Mexico City, Mexico, pp. 1168–1173 (2001). https://doi.org/10.1109/CCA.2001.974030
38. Arfken, G.B., Weber, H.J., Harris, F.E.: Mathematical methods for physicists (Seventh Edition). Academic Press, Boston (2013). https://doi.org/10.1016/c2009-0-30629-7